

**MASARYKOVA UNIVERZITA**  
**PŘÍRODOVĚDECKÁ FAKULTA**  
ÚSTAV TEORETICKÉ FYZIKY A ASTROFYZIKY

# **Bakalářská práce**

**BRNO 2020**

**DAVID ŠTEGNER**

**M A S A R Y K O V A**  
**U N I V E R Z I T A**  
PŘÍRODOVĚDECKÁ FAKULTA  
ÚSTAV TEORETICKÉ FYZIKY A ASTROFYZIKY

---

# **Vzorová spektra hvězd hlavní posloupnosti pro Ondřejovský Echelleťový Spektrograf**

Bakalářská práce

**David Štegnér**

Vedoucí práce: Mgr. Marek Skarka, Ph.D.      Brno 2020

# Bibliografický záznam

**Autor:** David Štegnér  
Přírodovědecká fakulta, Masarykova univerzita  
Ústav teoretické fyziky a astrofyziky

**Název práce:** Vzorová spektra hvězd hlavní posloupnosti pro Ondřejovský Echelletový Spektrograf

**Studijní program:** PřF B-FY Fyzika

**Studijní obor:** PřF FYZ Fyzika

**Vedoucí práce:** Mgr. Marek Skarka, Ph.D.

**Akademický rok:** 2019/2020

**Počet stran:** ix + 42

**Klíčová slova:** Ešeletová spektroskopie; Spektrum; Spektrální klasifikace; OES; IRAF

# Bibliographic Entry

**Author:** David Štegnér  
Faculty of Science, Masaryk University  
Department of Theoretical Physics and Astrophysics

**Title of Thesis:** Spectroscopic templates for the Ondrejov Echelle Spectrograph

**Degree Programme:** PřF B-FY Physics

**Field of Study:** PřF FYZ Physics

**Supervisor:** Mgr. Marek Skarka, Ph.D.

**Academic Year:** 2019/2020

**Number of Pages:** ix + 42

**Keywords:** Echelle spectroscopy; Spectrum; Spectral classification; OES; IRAF

# Abstrakt

Hlavním cílem této bakalářské práce bylo připravit spektrální atlas pro Ondřejovský Ešeletový Spektrograf (OES) připojený na 2m Perkův dalekohled v Ondřejově v České republice. Dle kritérií vycházejících z možností použitého přístroje jsme vybrali šestnáct hvězd hlavní posloupnosti ze všech základních spektrálních tříd OBAFGKM a pozorovali je během let 2018 a 2019. Získané snímky jsme pak upravovali a zpracovali pomocí programu IRAF a extrahovali spektra do 1-d formátu. U získaných spekter jsme analyzovali charakteristické oblasti každého spektrálního typu a potvrdili jejich spektrální typ nalezený v literatuře. Atlas může být použit k základní rychlé klasifikaci hvězd pořízených s OES.

# Abstract

The primary goal of this bachelor thesis was to prepare a spectral atlas for the Ondřejov Echelle Spectrograph (OES) mounted on the 2m Perek telescope located in Ondřejov, Czech Republic. We selected sixteen main-sequence stars of all the basic OBAFGKM spectral classes according to the criteria corresponding to the limits of the used instrument and observed them between 2018 and 2019. The obtained frames were then fully reduced by using software package IRAF and the spectra were extracted and combined to the 1-d format. We analyzed characteristic regions of each spectral type and confirmed the classification of stars in literature. The atlas can be used for a basic classification of stars observed by OES.



## ZADÁNÍ BAKALÁŘSKÉ PRÁCE

Akademický rok: 2018/2019

**Ústav:** Ústav teoretické fyziky a astrofyziky

**Student:** David Štegnér

**Program:** Fyzika

**Obor:** Fyzika

Ředitel Ústavu teoretické fyziky a astrofyziky PŘF MU Vám ve smyslu Studijního a zkušebního řádu MU určuje bakalářskou práci s názvem:

**Název práce:** Vzorová spektra hvězd hlavní posloupnosti pro Ondřejovský Echelletový Spektrograf

**Název práce anglicky:** Spectroscopic templates for the Ondřejov Echelle Spectrograph

**Oficiální zadání:**

Protože má každý spektrograf jiné charakteristiky, je pro efektivní práci dobré mít pro každý přístroj vlastní vzorová spektra hvězd různých spektrálních typů. Student vybere několik jasných hvězd hlavní posloupnosti pokrývajících co nejširší možný rozsah spektrálních tříd a pořídí spektra s Ondřejovským Echelletovým Spektrografem. Hlavním cílem je zpracování spekter a kontrola správnosti určení spektrálního typu zjištěná v literatuře.

**Jazyk závěrečné práce:** angličtina

**Vedoucí práce:** Mgr. Marek Skarka, Ph.D.

**Konzultant:** doc. Ernst Paunzen, Dr.

**Datum zadání práce:** 5. 12. 2018

**V Brně dne:** 3. 1. 2019

Souhlasím se zadáním (podpis, datum):

David Štegnér  
student

Mgr. Marek Skarka, Ph.D.  
vedoucí práce

prof. Rikard von Unge, Ph.D.  
ředitel Ústavu teoretické fyziky a  
astrofyziky

# Poděkování

Na tomto místě bych chtěl poděkovat svému vedoucímu Dr. Marku Skarkovi za vedení práce a jeho neutuchající podporu. Také bych rád poděkoval pozorovatelům ze Stelárního oddělení Astronomického ústavu Akademie věd České republiky za pořízení snímků použitých v této práci. V neposlední řadě děkuji svým prarodičům, kteří mi vždy ukazovali, že otevřená mysl je tím nejcennějším, co člověk má.

# Prohlášení

Prohlašuji, že jsem svoji bakalářskou práci vypracoval samostatně pod vedením vedoucího práce s využitím informačních zdrojů, které jsou v práci citovány.

I declare that I have elaborated my bachelor thesis independently using the information sources quoted in the paper.

Brno 1. června 2020

.....  
David Štegr

# Contents

<b>Introduction</b> .....	<b>1</b>
<b>Chapter 1. Stellar spectra</b> .....	<b>2</b>
1.1 A brief history of spectroscopy .....	2
1.2 Origin of the spectral lines .....	3
1.3 Phenomena affecting spectrum .....	4
1.3.1 Physical effects .....	4
1.3.2 Instrumental .....	6
1.4 Stellar classification .....	6
1.4.1 Brief history of stellar classification .....	6
1.4.2 Stellar classification nowadays .....	8
<b>Chapter 2. Observations</b> .....	<b>11</b>
2.1 Ondřejov Perek 2 m Telescope .....	11
2.1.1 Ondřejov Echelle Spectrograph .....	11
2.2 Selection of targets .....	11
2.3 Observation .....	14
<b>Chapter 3. Data process</b> .....	<b>16</b>
3.1 Frame pre-processing .....	16
3.2 Basic CCD frames reduction .....	17
3.3 Aperture extraction and flat fielding .....	18
3.4 Wavelength calibration .....	19
3.5 Normalization of the spectra .....	20
3.6 One dimensional spectrum production and its final corrections .....	20
<b>Chapter 4. OES spectral atlas</b> .....	<b>26</b>
4.1 Spectral type O – 10 Lac .....	27
4.2 Spectral type B – $\eta$ Aur, HD 14372 .....	28
4.3 Spectral type A – $\alpha$ Lyr, $\delta$ Leo, $\alpha$ Aql .....	28
4.4 Spectral type F – 49 UMa, HD 6301, HD 10874 .....	29
4.5 Spectral type G – HD 109358, HD 168009, HD 193664, HD 71148 .....	29
4.6 Spectral type K – 54 Psc, HD 84035 .....	30

4.7 Spectral type M – BD+63 869 .....	31
<b>Conclusions</b> .....	<b>33</b>
<b>References</b> .....	<b>34</b>
<b>Appendix</b> .....	<b>36</b>

# Introduction

*"Give me the place to stand, and I shall move the earth."*

Archimedes

*"Give me your spectrum, and I shall determine your spectral type."*

David Štegrner

Just as there are huge differences between stars, there are considerable differences in their spectra. The spectrum reflects the chemical composition (presence and amount of particular elements) of stars and the physical conditions in their atmospheres (temperature, pressure, surface gravity, rotation) and various types of movement including the proper motion of the star itself. Therefore, spectroscopy is the key tool for studying stars in the Universe. It can be said that just as the eyes are the windows to the human soul, the spectra are the windows to the soul of the star.

The spectra differ from star to star, but also from instrument to instrument. Each spectrograph has its own specifics (design, optics, size) and gives the spectrum a unique look. Even observing conditions and observation as well as the particular workflow in data reduction can affect the final look of the spectrum.

Over the decades, there have been several attempts to establish a classification of stars according to the look of their spectra. The temperature sequence appeared to be the best criterium and classical OBAFGKM classification was established. Since then, all the stars used this classification.

Although the spectral types are relatively well defined, the diversity of the instruments remains. This diversity raises the need to create not only general spectral atlases but also atlases designed for specific instruments. This thesis focuses on the creation of a spectral atlas for the Ondřejov echelle spectrograph mounted on the 2m Perek telescope in Ondřejov, Czech Republic. We used sixteen stars, which cover all the basic OBAFGKM spectral classes and investigated characteristic regions for the particular types.

The thesis is divided into four chapters. Chapter 1 summarizes the basic history and theory of spectra and their acquisition. Chapter 2 describes the instrument and the telescope that were used for the acquisition of the spectra. We also describe the selection process of the targets here. Chapter 3 outlines the process of data reduction and processing in IRAF software package. Chapter 4 shows the final spectra and their important details. Results of this thesis are summarized in the end.

# Chapter 1

## Stellar spectra

### 1.1 A brief history of spectroscopy

Spectroscopy is a fundamental exploratory tool in the fields of physics, chemistry, and astronomy, allowing us to investigate a structure of distant matter by studying electromagnetic waves radiated from it.

Spectrum means "image" or "apparition" in Latin. In the search for the history of spectroscopy, we have to go back to the 17th century and watch Isaac Newton doing his first optics experiments. Word spectrum was introduced to physics by Isaac Newton, referring to the range of colours produced, by refraction or diffraction on a prism, from a beam of light (Newton, 1671). Thanks to the progress in optics, especially in the study of prisms, he could perform systematic observations of the solar spectrum and found that sunlight is made up of a mixture of all the colours of the rainbow (Gray & Corbally, 2009).

Another name that must not be forgotten is Joseph von Fraunhofer. He conducted experiments replacing a prism with a self-made diffraction grating as the source of wavelength dispersion in his spectrometer. The interference achieved by a diffraction grating improved the spectral resolution against a prism. He made this grating from equally spaced thin wires.

There exists a simple relation between the diffraction angle and the wavelength during interference maxima

$$l = d \sin \theta = m\lambda, \quad (1.1)$$

where  $l$  is the path difference of light between two slits,  $d$  is the distance between the two parallel slits,  $\theta$  represents diffraction angle, the integer  $m$  represents an order of the maximum, and  $\lambda$  stays for wavelength. Fraunhofer knew the grating period of his grating and was able to measure and list the wavelengths of the observed absorption lines (Appenzeller, 2013). He also found several dark lines in a continuous spectrum of the Sun, dark lines that remained a mystery for the next 30 years (Gray & Corbally, 2009).

A significant breakthrough in the field of spectroscopy was made in the 1860s thanks to physicist Gustav Kirchhoff and chemist Robert Bunsen. They were able to find a connection between chemical elements and their spectra. Bunsen created the Bunsen burner. Kirchhoff later suggested that similarly coloured flames could be differentiated by looking at their emission spectra through a prism. When he shone bright light through such

flames, the dark lines in the absorption spectrum of the light corresponded in wavelengths, with the wavelengths of the bright, sharp lines characteristic of the emission spectra of the same test materials (e1, 2018). Kirchhoff and Bunsen also definitively established the link between absorption and emission lines, including attributing solar absorption lines to particular elements based on their corresponding spectra. Kirchhoff continued to contribute fundamental research on the nature of spectral absorption and emission, including what is now known as Kirchhoff's Law of Thermal Radiation (Kirchhoff & Bunsen, 1860).

Kirchhoff's Law describes the equivalent ratio of emissive and absorptive power of rays with the same wavelength at thermal equilibrium:

$$\varepsilon_{\lambda}(T) = \alpha_{\lambda}(T), \quad (1.2)$$

where the absorbability  $\alpha_{\lambda}(T)$  is the effectiveness in absorbing radiation energy for a particular wavelength  $\lambda$  at given temperature  $T$ . The emissivity  $\varepsilon_{\lambda}(T)$  is defined as the ratio of emitted energy to the amount that would be radiated by the perfect black body. Kirchhoff's applications of this law to spectroscopy are summarized in three laws of spectroscopy (Grossová, 2016):

1. A solid matter, liquid matter, or dense gas excited to emit light will radiate at all wavelengths and thus produce a continuous spectrum.
2. A low-density gas excited to emit light will do so at specific wavelengths and this produces an emission spectrum.
3. If light composing a continuous spectrum passes through a cool, low-density gas, the result will be an absorption spectrum.

## 1.2 Origin of the spectral lines

As we know, atoms consist of a heavy nucleus with a positive charge and bound electrons with a negative charge. Electrons in atoms can be described both as particle and wave. This dualism can be sufficiently described by quantum mechanics, which we demonstrate on hydrogen with one proton as a nucleus which is orbited by one electron. The problem of the classical theory is that the energy of an atom can not be arbitrary and must have certain values. We have to consider, that electrons in atoms do not behave as classical particles but as stationary waves. Following the pattern of quantum mechanics, we have to solve the Schrödinger equation, for an electron trapped in a potential well with the Coloumbic potential energy

$$E_p = \frac{1}{4\pi\epsilon_0} \frac{-eq}{r}, \quad (1.3)$$

where  $r$  is the distance between electron and positive nucleus,  $\epsilon_0$  is the permittivity of vacuum,  $e$  is the elementar charge, and  $q$  is the charge of a proton. We can get energy of quantum states of electron by solving Schrödinger equation for hydrogen:

$$E_n = -\frac{m_e e^2 q^2}{8\epsilon_0^2 h^2} \frac{1}{n^2} = -\frac{13.5984\text{eV}}{n^2} \left(\frac{q}{e}\right)^2 = \frac{E_1}{n^2}, \quad (1.4)$$

where  $E_n$  is energy of the  $n$ -th state,  $m_e$  is mass of an electron,  $h$  is Planck constant, and  $E_1$  is energy of the first energy level, the ground state level. As we find out from the above, value of the ground state is  $E_1 = -13.5984$  eV, values of other levels are dependent on this value by equation:

$$E_n = \frac{E_1}{n^2}, \quad (1.5)$$

where  $n$  stands for the order of the energy state, and  $E_n$  stands for energy of the  $n$ -th state. Atoms with more electrons have a similar structure of allowed energy levels that is characteristic for each element. The characteristic basic energetic level that represents the smallest possible energy can be found every time. Above that, there is an infinite number of discrete energetic levels, that set ends when the energy reaches the level where the electron leaves the atom. Finally, the line spectrum arises from passing between allowed states with different energies. This passing is called bound-bound transition and is accompanied by photon absorption or emission with energy equal the difference between the two states.

There are several specific spectral series, e.g. Paschken series or Balmer series. Passing in individual series always ends on a specific level and begins on some of the upper levels. Spectral lines in the Balmer series are labelled with greek alphabet letters, for example,  $H\alpha$  means passing between the 3rd and the 2nd level in the hydrogen atom. The wavelength of spectral lines or of every other photon emitted by passing between different energy levels can be calculated by the quasiclassical equation postulated by Balmer for hydrogen:

$$\frac{1}{\lambda} = R \left( \frac{1}{n_{\text{final}}^2} - \frac{1}{n_{\text{initial}}^2} \right), \quad (1.6)$$

where  $\lambda$  means the wavelength,  $n_{\text{final}}$  and  $n_{\text{initial}}$  stands for final, and initial energy levels, and  $R = 1.0974 \times 10^7 \text{ m}^{-1}$ , which is the Rydberg constant. This equation can be generalized for every particle (Mikulášek Z., Krtička J., 2005).

## 1.3 Phenomena affecting spectrum

Current spectral classification is mainly based on effects caused by the temperature of a star, but the temperature is not the only factor. The importance of the other influencing factors that can lead to systematic effects in classification will be discussed in this section.

### 1.3.1 Physical effects

The number of nonionized atoms is getting lower with increasing temperature. This can be demonstrated by Saha equation, that describes the problem of ratio between number of the  $(i+1)$ -times ionized atoms ( $N_{i+1}$ ) to number of the  $i$ -times ionized atoms ( $N_i$ )

$$\frac{N_{i+1}}{N_i} = \frac{2}{N_e} \frac{Z_{i+1}}{Z_i} \left( \frac{2\pi m_e kT}{h^2} \right)^{\frac{3}{2}} e^{-\frac{E_i}{kT}}. \quad (1.7)$$

In the above equation 1.7,  $N_e$  is concentration of free electrons,  $Z_i$  is partition function for corresponding degree of ionization,  $k$  is Boltzman constant, and  $T$  stands for temperature. Therefore, lines from Balmer series are most significant for 9900 K, and getting less apparent with higher temperature due to a decrease of neutral atoms.

As a star rotates, some parts are approaching, and others are moving away. The lines are broadened thanks to the Doppler effect caused by rotation. Broadening depends on rotation rate and the angle of inclination of the axis of rotation to the line of sight. Therefore stellar rotation rate is calculated using the broadening effect. In general, the hottest stars rotate the fastest with periods as fast as 4 hours. Sun-like stars rotate relatively slowly at about once every 27 days (e2, 2018).

The difference in the width of lines can lead to confusions when comparing standard stars and investigated stars. Therefore, researchers used parallel classification standards with high and low rotatig velocity in the past. However this only works for some types of stars, for example Gray & Garrison (1987) system for A-type stars. The rotational broadening is most aparent in late B- type stars (Gray & Corbally, 2009).

Rotation also affects the physical properties of stellar atmospheres via centrifugal force which causes that gravity and effective temperature vary through the surface. It was shown that equator has a lower effective temperature and gravity than can be found in the polar regions. Thus, there is a slightly different composite spectrum from every aspect angle. The rotation can also affect the position of a star on the H-R diagram. The best example of this phenomenon is probably Vega. It was shown by Petrie (1964), that Vega is overluminous by 0.7 magnitudes for its spectral type. After suggestions from Gray (1985) and Gray (1988), it was later shown that Vega is a rapid rotator seen pole-on, by high-resolution spectroscopy (Gulliver et al., 1991) and by optical interferometry (Aufdenberg et al., 2006; Peterson et al., 2006).

Surface gravity also affects the spectra. As direct measurements of gravity are not always possible, we must trust in indirect measurements. For example, the effects of pressure are the best we have to determinate the surface gravity because increasing gravity is projected in an increase of all kinds of pressures. Contributions of electron and gas pressure are the most important in this context. Because electron pressure relies on the ionization level of the matter, the presence and strength of particular lines are different in different stars (Catanzaro (2014)). For example, the Fe lines are mostly ionized in F-type stars. Thus, Fe I lines are insensitive to the gravity, and Fe II lines are sensitive. Lines from O I are also good indicators of gravity because oxygen is neutral at F-type temperatures. The lines of the giant are narrower than the lines of the dwarf.

Talking about strong lines in cool stars, sodium doublet and hydrogen Balmer lines are narrower in the spectrum of a giant star than in the spectrum of a dwarf star. Contrary to sodium dublet, Ca II K line shows inverse behaviour – it broadenes with decreasing surface gravity (Catanzaro, 2014).

Radial velocities of stars effect the spectra, by shifting the spectral lines in the horizontal axis due to Doppler effect (blue and red shift). We can measure the approximate radial velocities  $v_{\text{rad}}$  from the position of spectral lines using a simple relation

$$v_{\text{rad}} = \frac{\lambda_{\text{obs}} - \lambda_0}{\lambda_0} c, \quad (1.8)$$

where  $\lambda_{\text{obs}}$  is the observed wavelength of a spectral line,  $\lambda_0$  is the laboratory wavelength of the same spectral line, and  $c$  is the speed of light.

### 1.3.2 Instrumental

The properties of the instrument influence the spectrum. In spectroscopy, the resolving power of an instrument using slits is

$$R = \frac{\lambda}{\Delta\lambda} = mN = \frac{l}{\Delta l}, \quad (1.9)$$

where  $\Delta\lambda$  is the difference between two wavelengths that can be resolved,  $N$  is a number of equidistant slits (grooves in 1.10), and  $\Delta l$  is the difference between interference maxima. Thus,  $R$  depends only on the number of interfering beams and on the order ( $m$ ) of the interference. Using grating with grooves, we can express  $R$  as

$$R = \frac{\lambda}{\Delta\lambda} = mN = \frac{Nd}{\lambda}(\sin i + \sin j), \quad (1.10)$$

because  $l = d(\sin i + \sin j)$  and  $j$  is diffraction angle,  $i$  is inclination angle, and  $d$  is the distance between two grooves (Appenzeller, 2013).

The individual orders partially overlap, this means that in high orders  $m$  different segments of spectra are projected. If we succeed in splitting these segments we can get large portion of spectrum at once. This is the principle of echellette spectroscopy, which is shown in Fig. 1.1. Cross-disperser separates the individual images of the orders and projects them above each other. Light is then divided into a ladder-shaped structure called echellogram because the french word for a ladder is "échelle" (e3, 2018). With the echelle spectrographs, we can achieve high resolving power. Echelle gratings usually have grating periods  $d$  between  $3 \mu\text{m}$  and  $40 \mu\text{m}$  and operate at diffraction orders  $m$  bigger than 40. Components of spectrometer used in this thesis will be discussed later in the next chapter.

Each astronomical measurement collects certain amount of energy  $E_t = F_\nu A \Delta\nu \Delta t \xi$ , that is given by spectral flux  $F_\nu$ , the light collection surface of the telescope  $A$ , frequency bandwidth  $\Delta\nu$ , the integration time  $\Delta t$  and total instrument efficiency  $\xi$ . The total number of captured photons for monochromatic light is then  $n_{\text{phot}} = \frac{E}{h\nu}$ , where  $h\nu$  represents energy of one photon. The statistic mean error  $\Delta n = \sqrt{n_{\text{phot}}}$  is called photon noise. Detector also records sky background  $n_{\text{sky}}$ , that increases the noise. Thus, signal to noise ratio

$$\frac{S}{N} = \frac{n_{\text{object}}}{\sqrt{n_{\text{object}} + n_{\text{sky}}}} \quad (1.11)$$

is very useful for determination of quality of spectra. The signal to noise ratio can be improved by increasing the exposure time.

## 1.4 Stellar classification

### 1.4.1 Brief history of stellar classification

One of the first attempts to classify stars by its spectra was made by Ernst Rutherford. He separated them into three groups:

1. Sun-like stars with many bands and lines.
2. Stars like Sirius, which are white stars with lines, unlike the Sun.
3. Stars like Riegel, which are white but show no lines.

We can see a clear analogy with the generally adopted system currently in use: class 1 represents late-type stars, class 2 is equivalent to late-B to early-F stars and class 3 equals to OB stars [1.4.2](#).

Another significant attempt to classify the spectra was made by Angelo Secchi. He tried to divide spectra into two groups, the early and the late-type stars. Then he added another three types of spectra to his classification because the first two groups were not sufficient enough. First, he added a group that would be considered as today's M-type stars. The next two groups were the carbon stars, that could be represented as faint red stars today and some emission-line stars. He was able to classify at least 4000 stars and thereby illustrated the first principle of classification, that you need as many specimens as possible. His classification wasn't faultless, but it was one of the crucial milestones in stellar classification ([Gray & Corbally, 2009](#)).

Many of later researchers like Herman Carl Vogel were using Secchi's classes in their work. However, the discovery of helium both in stars and on the Earth made many discrepancies in Vogel's classification system. Vogel's work helped Norman Lockyer to divide the spectra of giants and supergiants from those of dwarfs. One of the most complex classification systems until then was brought by amateur astronomer F. McLean in 1897. His system was able to include stars with neutral helium absorption. It was a combination of Secchi's and Vogel's systems. His classes corresponded to B, A, F, G+K, M and carbon stars of the currently used system, which is discussed further in the text. McLean's remarkable contribution to the field of spectral classification was to find that some lines in "helium stars" corresponded to the spark spectra for oxygen ([Gray & Corbally, 2009](#)).

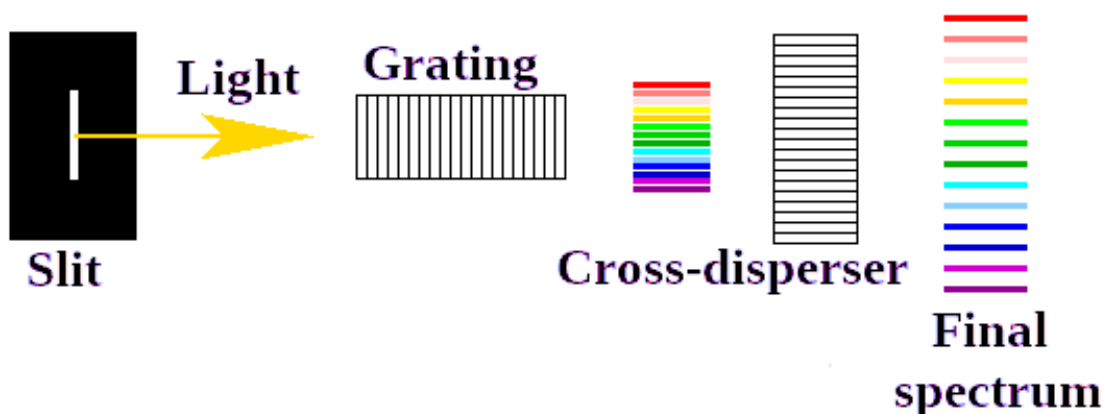


Figure 1.1: Figure showing the evolution of light as it passes through an echelle spectroscopy ([e3, 2018](#)).

## 1.4.2 Stellar classification nowadays

### Temperature dependency

Harvard astronomers E. Pickering, W. Fleming, and A. Maury introduced a recently well known spectral sequence: O B A F G K M, which goes from the highest temperature to the lowest. Harvard classification stands on this strong bond between spectra and temperature [1.3.1](#). Two groups L and T that stand the lowest temperatures were added over the years. Each letter class is then subdivided using a numeric digit with 0 being hottest and 9 being coolest ([Gray & Corbally, 2009](#)).

- O stars are rare but very luminous and massive. They have temperature above 30000K. Classification of O-type stars is based on the ratio between He I (4471)<sup>1</sup> line and He II line that varies in favour of He II (4541) with decreasing temperature. He I (4387) line dominates the ratio between He I (4387) and He I (4144) lines till the O9 type. Increasing detectability of the Si II (4128-4130) indicates decreasing the effective temperature of a star. HD 46223 is often used as an O-type standard star ([Gray & Corbally, 2009](#)).
- B stars have temperatures between 10000 and 30000K. The classification as B-type is based on the behaviour of the He I spectrum with maximum intensity for the main sequence B2 stars and on strengthening Balmer lines through B stars to A stars with the maximum at A2 type. Early B-type stars are classified by the ratio of Si II (4128-4130) and Si III (4552) lines, that varies in favour of Si II (4128-4130) with decreasing temperature. Also, the Mg II (4481) line, that appears in spectral type B0 and strengthens with lower temperatures indicates B-type star ([Gray & Corbally, 2009](#)).
- A-type stars are usually fast rotators. Possibility of rotation has to be considered during classification. The A-type stars show strong Balmer hydrogen lines and almost no He I lines, which can also be used for their identification. Hydrogen Balmer lines are weakening from A2 towards lower temperatures. H $\delta$  (4102) line weakens with decreasing temperature, so comparing it with H $\epsilon$  (3970) line helps us with a classification of suspected K-type star. Ca II K-line (3934) is rapidly strengthening towards later types similar to the metallic lines ([Gray & Corbally, 2009](#)).
- F-type stars are stars with temperature about 7500 K ([e4, 2020](#)). Crucial for their classification are hydrogen lines that weakens with decreasing temperature. Strenght of Ca II K (3934) line is mostly constant, but general metallic lines continue their strengthening from the A9 level to the later types. For example, the Ca I (4226), and Fe I (4046) lines grow with decreasing temperature ([Gray & Corbally, 2009](#)).
- G-type stars with their temperature around 6000 K ([e4, 2020](#)) are similar to our Sun and the most likely stars to have habitable planets. Hydrogen Balmer lines are slowly weakening with higher temperatures, and metallic lines start to increase. For

---

<sup>1</sup>All wavelengths are rounded and given in angströms [Å]. From now on, the wavelengths will be given in brackets without a unit.

example, the Ca I (4226), Fe I (4046), Fe I (4144), Fe I (4383) and Mg I (5167, 5172, 5183) lines grow with decreasing temperature and indicate the G-type stars (Gray & Corbally, 2009).

- K-type stars are slightly cooler than the Sun and have extremely weak hydrogen lines. Spectra are dominated by neutral metals (e5, 2018). Thus, K-type stars can be identified by ratios of Fe I, Ca I metallic lines and hydrogen Balmer lines, because hydrogen lines are getting weaker with decreasing temperature. Cr I (4254, 4275, 4290) triplet increases its strength through later types (Gray & Corbally, 2009).
- M-type stars take a significant part of the stars in our neighbourhood. Hydrogen core burning (main sequence) M-type stars have in general low brightness that none is bright enough to be seen with the naked eye (e5, 2018). Na I doublet (5890, 5896) broadening can be a good indication of M type star (e4, 2020). Fe I (4383) and Cr I (4254, 4275, 4290) triplet metallic lines are losing their strength with decreasing temperature. Strengthening of TiO (4804, 4955, 5166) lines also indicate M type star (Gray & Corbally, 2009).

### Luminosity classes and Morgan-Keenan classification

The spectra of the stars inform, among other things, about the surface gravitational acceleration.

$$g = \frac{GM}{R^2}, \quad (1.12)$$

where  $G$  is the gravitational constant,  $M$  stands for mass and  $R$  stands for the radius of a star see sect. 1.3.1. If the gravitational acceleration is high, the atmosphere of the star is thin and relatively dense. Spectral lines are broadened due to the effect of pressure. On the other hand, the spectral lines of stars with low surface gravity acceleration are deep and narrow.

Since the 20th century, the two-degree Morgan-Keenan (M-K) classification is used. The M-K classification complements the classification mentioned above by so-called luminosity class, which locate the star in the HR diagram (Fig. 1.2). Luminosity classes are Ia - bright supergiants, Ib - supergiants, II - bright giants, III - giants, IV - main sequence stars, VI - subdwarfs, VII - white dwarfs (Mikulášek Z., Krtička J., 2005).

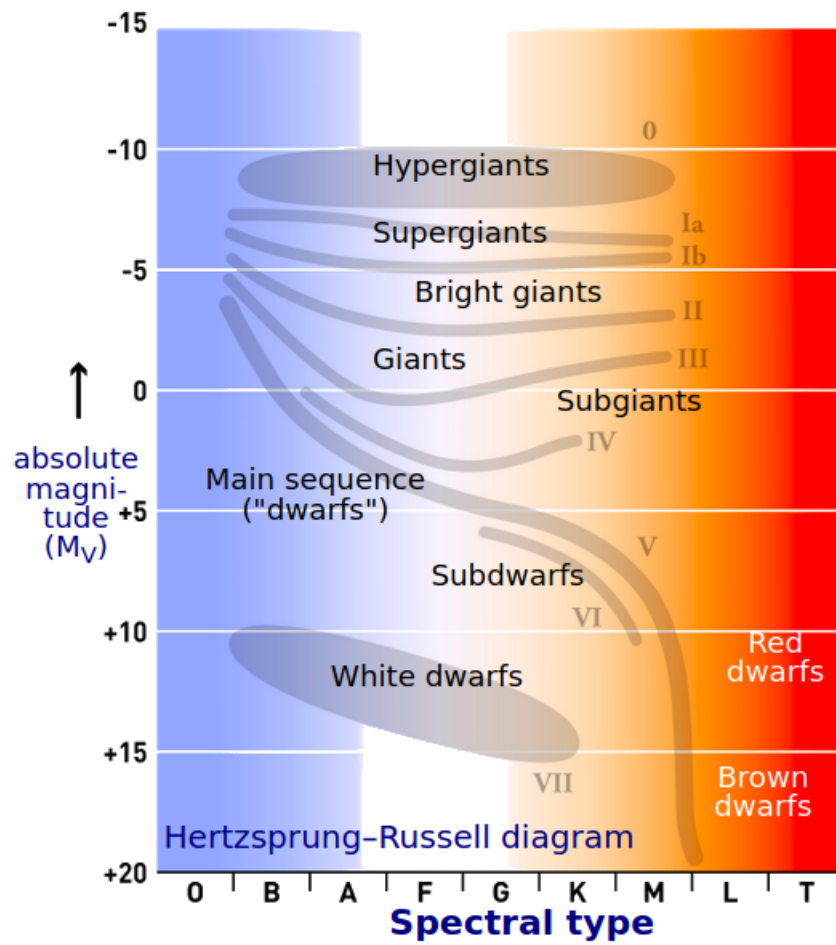


Figure 1.2: Figure showing a relation between luminosity classes and temperature types (e5, 2018).

# Chapter 2

## Observations

### 2.1 Ondřejov Perek 2 m Telescope

The 2-metre telescope was constructed in 1966 by Carl Zeis Jena company. The telescope is attached to the equatorial mount on the first floor of the observatory (Fig. 2.1). Parabolic primary mirror with a 2m diameter and focal ratio of 1:4.5 focuses light to the secondary convex hyperbolic mirror with 0.58 m diameter. This set gives effective focal length of 63.5m and effective focal ratio of 1:32. The telescope was primarily used for spectroscopy since its assembly in 1967. The light is directed to the coude focus on the ground floor and goes either to the single-slit spectrograph or to Ondřejov Echelle Spectrograph (Fig. 2.1).

#### 2.1.1 Ondřejov Echelle Spectrograph

The optical design of OES (Fig. 2.2) was inspired by Heidelberg Extended Range Optical Spectrograph (HEROS) built in 1994 by A. Kaufer in Germany. OES was constructed by research team under the lead of P. Koubský in 2000. OES is an echelle spectrograph with a slit as a source of point light, placed in the isolated room next to the observing and operation center (see panel b of Fig. 2.1). The resolving power of the spectrograph is 51600 at 5000 Å (Koubský et al., 2004).

The optical design of OES is in Fig. 2.3. The light coming from the telescope goes through the slit A in the coude focus and is reflected and collimated by spherical collimator B. After that, the light beam goes to the echelle grating positioned in a blaze angle of 69 degrees (21 degrees from the horizontal plane). Light beam is then focused by parabolic mirror D to plane mirror E, that sends the beam to be collimated by parabolic collimator F. Light beam is then divided to the spectral orders by prism G used as a cross-disperser and captured by camera H. The chip is cooled with liquid nitrogen to a temperature of  $-110^{\circ}\text{C}$ .

### 2.2 Selection of targets

When selecting the object, we followed criteria that can be divided into two groups: Observational and physical. The observational criteria were brightness and position of the star

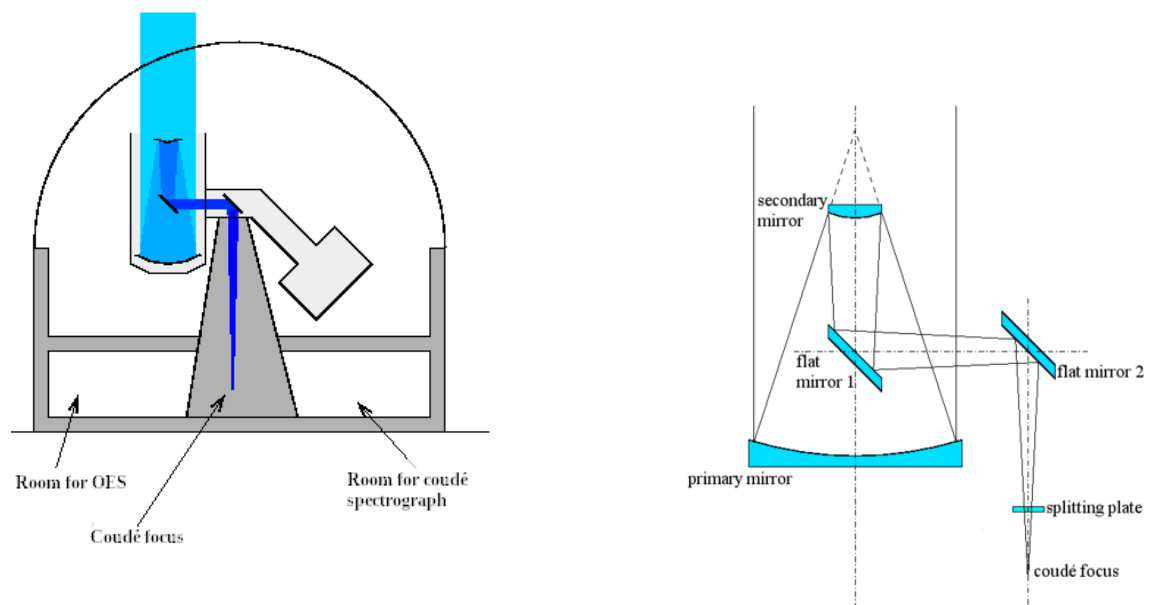
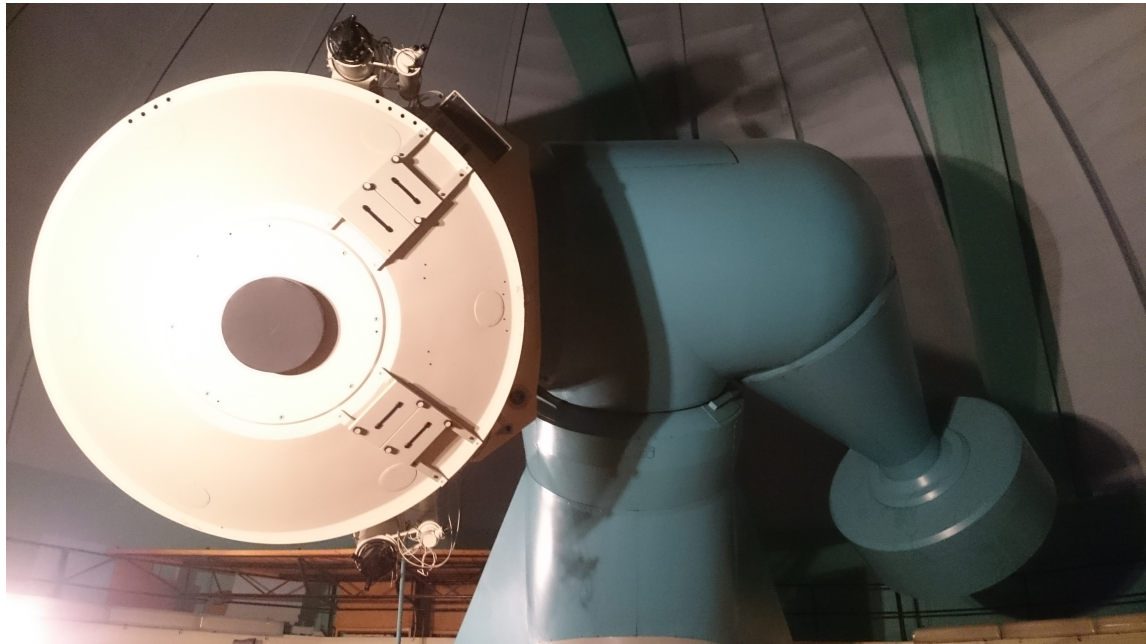


Figure 2.1: The overall view of the Perek 2m telescope (top panel), the scheme of the building (bottom left panel) (e3, 2018) and the optical scheme of the telescope (bottom right-hand panel) (e6, 2019).

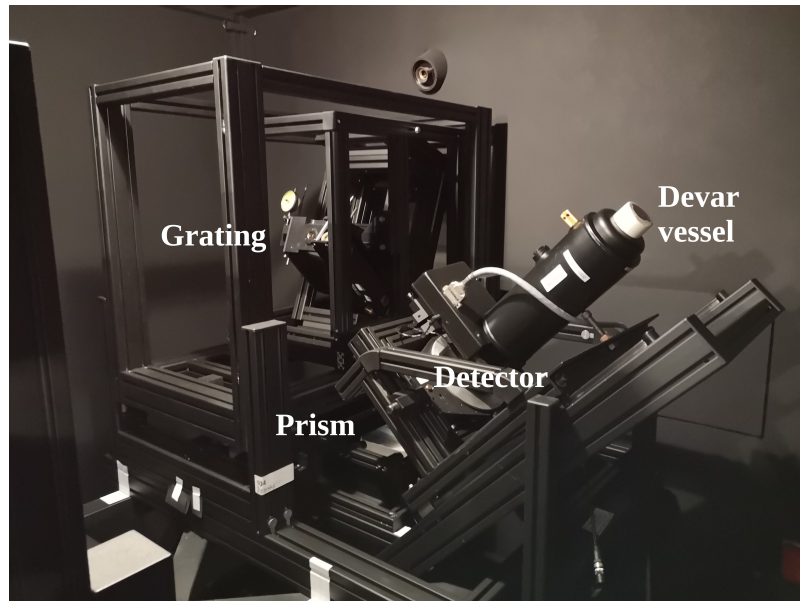


Figure 2.2: Photo of the OES. The light comes from behind the whole structure. We see the detector, Devar vessel, grating and prism in the picture.

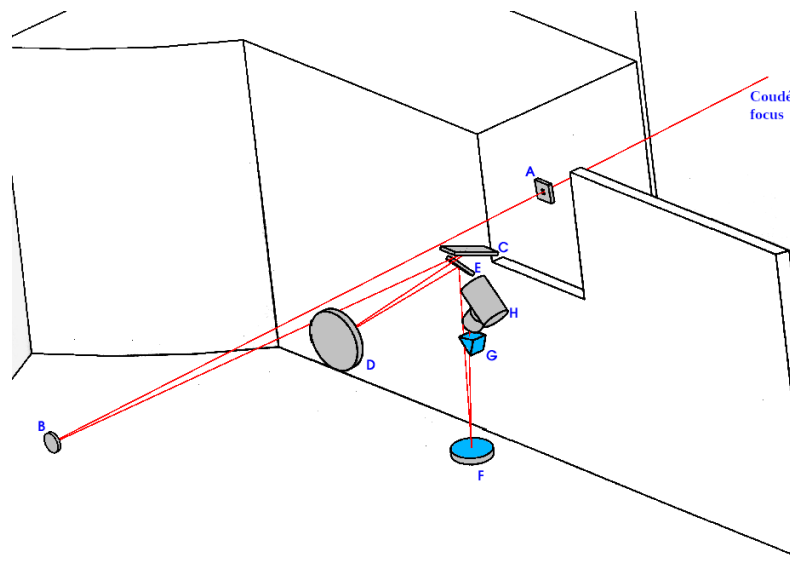


Figure 2.3: OES scheme including the path of the light. A - Slit, B - Spherical collimator ( $d = 150$  mm,  $f = 4600$  mm.), C - Echelle grating (54.5 engravings per millimeter and the size 154x408 mm.), D - Parabolic mirror ( $d = 450$  mm and  $f = 1628$  mm), E - Plane mirror, F - Parabolic collimator ( $d = 300$  mm,  $f = 1086$  mm, with image of pupil 100 mm in diameter), G - Prism (cross-disperser), H - Camera (e3, 2018).

on the sky. Brightness had to be higher than 9 magnitudes in visual, which was determined by the limits of the optical system in Ondřejov.

Stars had to be observable from autumn to spring to be able to fulfill the goals of the thesis in a given time. The physical criteria included covering the full range of spectral types (OBAFGKM). Because we want to cover the most extensive range of spectral types an ideal approach would be to find and observe at least two stars of each spectral type. We consider only main sequence stars and completely omit other luminosity classes because their spectra are affected by different physical phenomena. The main sequence luminosity class is labeled with Roman numeral V in Fig. 1.2. Selected stars are listed in Table 2.1.

Table 2.1: Column "NAME" shows the identification of the stars. Columns "RA" and "DEC" show stellar equatorial coordinates of the star. Column  $V$  shows flux in visual in magnitudes. Column  $B - V$  shows the difference between flux in blue and visual in magnitudes. Column "Sp. Type" shows the spectral type of the stars presented in the literature. Column "Ref" shows source of values for the particular star. C76 is Cowley (1976). G09 is Gray & Corbally (2009). H91 is Hoffleit & Jaschek (1991).

NAME	RA	DEC	$V$ [mag]	$B - V$ [mag]	Sp. Type	Ref
10 Lac	22 39 15.68	+39 03 00.97	4.88	-0.21	O9V	G09
$\eta$ Aur	05 06 30.89	+41 14 04.11	3.18	-0.18	B3V	G09
HD 14372	02 20 41.51	+47 18 38.92	6.15	-0.09	B5V	H91
$\alpha$ Lyr	18 36 56.34	+38 47 01.28	0.03	0.00	A0V	G09
$\delta$ Leo	11 14 06.50	+20 31 25.39	2.53	0.15	A4V	H91
$\alpha$ Aql	19 50 47.00	+08 52 05.96	0.77	0.22	A7V	H91
49 UMa	11 00 50.42	+39 12 43.48	5.06	0.24	F0V	C76
HD 6301	01 04 27.62	+29 39 31.63	6.20	0.43	F5V	C76
HD 10874	01 47 48.01	+46 13 47.10	6.32	0.44	F6V	C76
HD 109358	12 33 44.54	+41 21 26.92	4.25	0.66	G0V	C76
HD 168009	18 15 32.46	+45 12 33.54	6.30	0.63	G1V	H91
HD 193664	20 17 31.33	+66 51 13.28	5.98	0.66	G3V	C76
HD 71148	08 27 36.78	+45 39 10.76	6.39	0.69	G5V	H91
54 Psc	00 39 21.81	+21 15 01.72	5.88	0.83	K0V	G09
HD 84035	09 43 25.66	+42 41 29.62	8.25	1.35	K5V	(e7, 2018)
BD+63 869	09 56 08.67	+62 47 18.47	9.18	1.5	M0V	H91

## 2.3 Observation

Observation was accomplished in cooperation with the staff of the Czech astronomical institute in Ondřejov. All the 16 selected stars were observed during 10 nights (Table 2.2). Observations were made by M. Skarka, E. Kortusová, J. Dvořáková, M. Špoková, P. Kabáth, M. Blažek, L. Řezba, R. Novotný, J. Fuchs. Additional informations about observations used in this thesis are listed in Table 2.2.

Table 2.2: Column "STAR" shows the stars from Table 2.1. Column "DATE" shows the date of the observation. The column "Observers" shows observers, that observed during that night including M. Skarka (MS), E. Kortusová (EK), J. Dvořáková (JD), M. Špoková (MŠ), P. Kabáth (PK), M. Blažek (MB), L. Řezba (LŘ), R. Novotný (RN), J. Fuchs (JF). Column "Exp" shows exposure time used per frame during the observation. Column "Moon" shows the distance of the Moon from the observed star in degrees. "SNR" represents the signal to noise ratio.

STAR	DATE	Observers	Exp [s]	Moon deg	SNR
10 Lac	Nov, 6 2018	EK	600	120	107
$\eta$ Aur	Oct, 22 2018	EK	600	70	167
HD 14372	Nov, 16 2018	JD, RN	900	85	48
$\alpha$ Lyr	Oct, 21 2018	EK	60	80	230
$\delta$ Leo	Nov, 16 2018	JD, RN	600	65	59
$\alpha$ Aql	Nov, 16 2018	MŠ, JF	120	45	179
49 UMa	Mar, 22 2019	PK, RN	1200	55	193
HD 6301	Nov, 16 2018	JD, RN	900	50	51
HD 10874	Nov, 16 2018	MŠ, JF	900	70	49
HD 109358	Apr, 4 2018	MS, RN	600	75	157
HD 168009	Aug, 18 2018	LŘ	600	65	75
HD 193664	Mar, 3 2019	MB, RN	600	85	110
HD 71148	Nov, 11 2018	JD, RN	900	145	52
54 Psc	Oct, 21 2018	MB, RN	900	150	50
HD 84035	Mar, 3 2019	MB, RN	600	150	37
BD+63 869	Mar, 21 2019	MB, RN	3600	70	33

# Chapter 3

## Data process

OES produces files in the FITS (Flexible Image Transport System) format. A typical CCD scientific object frame produced by OES is shown in Fig. 3.1. Bias frames, flat field frames, and calibration frames for wavelength calibration are shown in Fig. 3.2. Data process consist of the frame pre-processing (Sect. 3.1), basic CCD frame reduction (Sect. 3.2), aperture extraction and flat fielding (Sect. 3.3), wavelength calibration (Sect. 3.4), normalization (Sect. 3.5) and production of one dimensional spectrum. (Sect. 3.6).

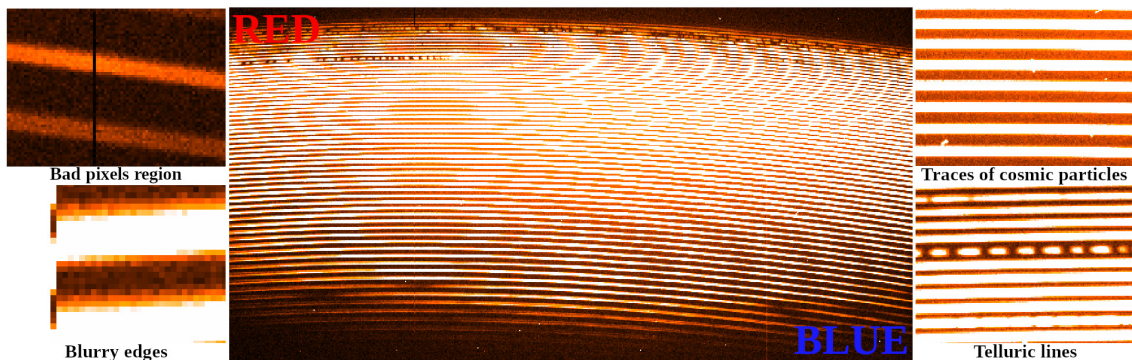


Figure 3.1: CCD frame showing the echellogram of 49 UMa taken on October 21, 2018. Wavelength increases from bottom to top and from right to the left. Bad pixel, blurry edges and traces of cosmic particles are shown in the details. Region of telluric lines are also shown.

We used the widely used software package Image Reduction and Analysis Facility (IRAF), written by National Optical Astronomy Observatory (NOAO) (e8, 2020) as a primary tool for the data reduction and extraction of spectra. We used DS9<sup>1</sup> made by Smithsonian Astrophysical Observatory (SAO) for displaying the frames.

### 3.1 Frame pre-processing

All frames need to be slightly corrected before the actual scientific process. The CCD chip and the optical path (Fig. 2.1, Fig. 2.3) have their flaws, which produce bad pixels

<sup>1</sup><http://ds9.si.edu/site/Home.html>

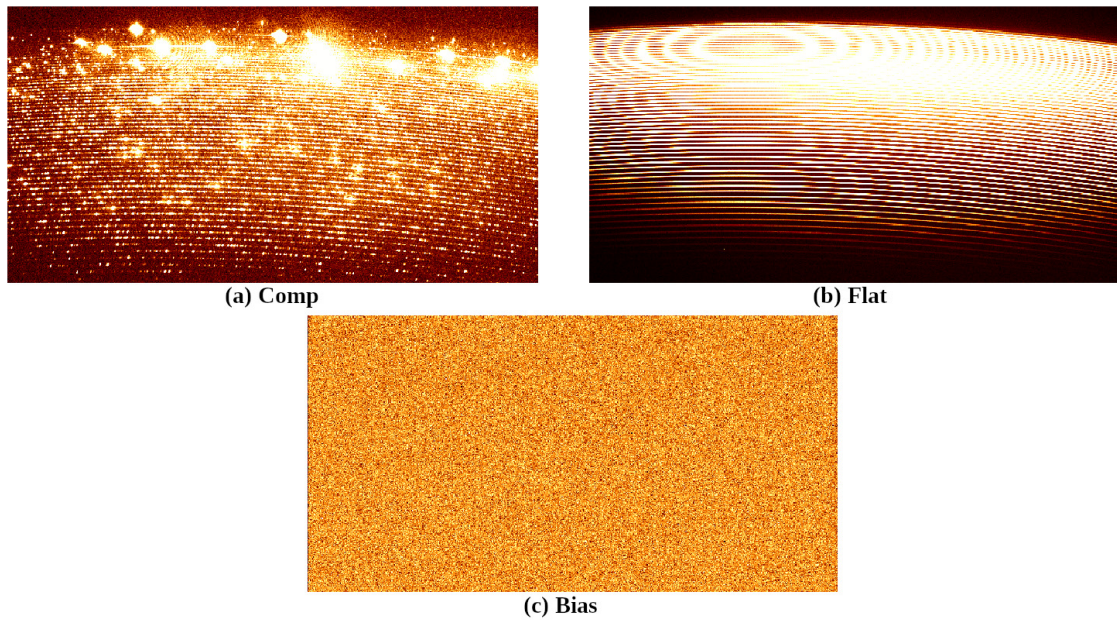


Figure 3.2: All calibration frames. ThAr frame in panel (a), flat frame in panel (b) and bias frame in panel (c).

and blurry edges on the frame, see details in Fig. 3.1. We need to replace the known bad regions by linear interpolation along lines or columns using the nearest good pixels. Bad pixels and columns must be identified by the user and defined in a bad pixel mask file. This correction is made by the task "fixpix" in IRAF. The used settings of task "fixpix" are in the appendix in Fig. 4.9.

There are cosmic particles flying around us all the time. These particles can leave unwanted traces on the frames (see Fig. 3.1). The longer the exposure and the activity of the Sun, the more cosmic hits appear on the frames. The procedure of their removal must not be applied on the comparison thorium argon (ThAr) frames, because the narrow emission lines can be treated as cosmic hits by the algorithm. The similarity of the ThAr emission lines and cosmic hits can be seen if we compare bright dots in the top-left panel of Fig. 3.2 and 3.1. This procedure is performed using task "cosmicrays" in IRAF. We removed the blurry edges by cutting the frame of 5 pixels from the right edge, 8 pixels from the left edge. We then removed 500 pixels from the bottom edge, and 300 pixels from the top edge to get rid of unnecessary parts of the frames. We removed all the regions by task "imcopy". Frame proportions change from 2048x2048 pixels to 2035x1250 pixels.

## 3.2 Basic CCD frames reduction

We made two sets of calibration frames, bias frames, and flat frames. Bias frames are made with a zero exposure time. We capture bias frames to remove base level of readout noise, that occurs during reading the values of each pixel on the sensor. Flat frames are made to reduce the influence of the optical system including the CCD camera to reduce the inhomogeneous illumination of the chip and pixel-to-pixel variation. We usually make

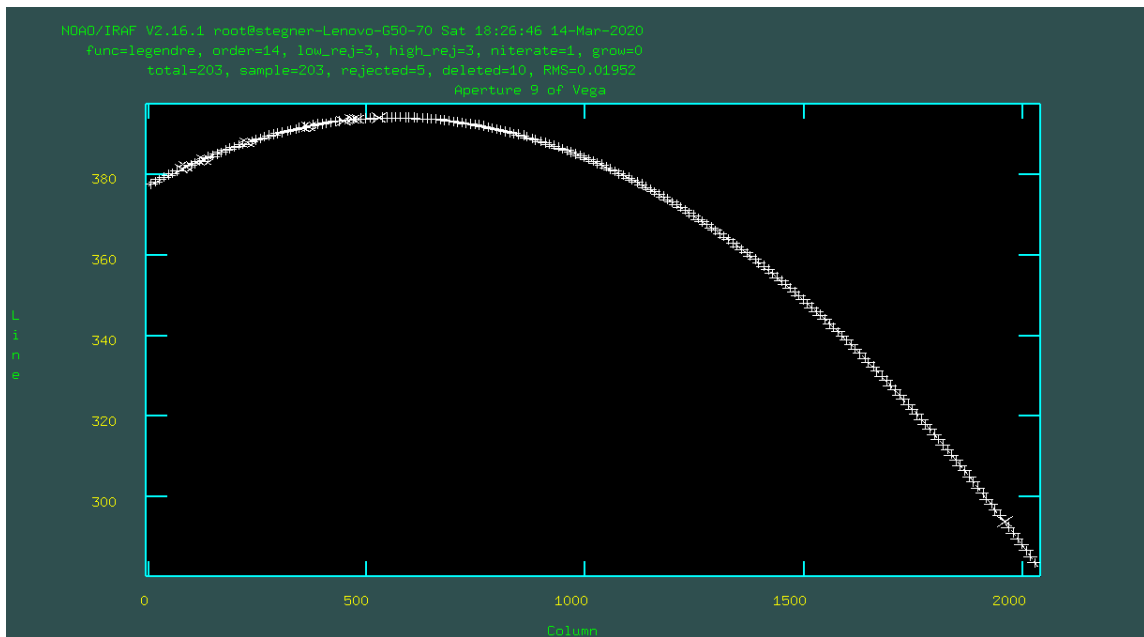


Figure 3.3: Tracing aperture 9 of  $\alpha$  Lyr frame in IRAF by task "apall".

from 10 to 20 both flat frames and bias images, that need to be combined into one "master" frame. Master calibration frames are made by task "imcombine". You can find settings of this task in Fig. 4.10 in the appendix. A set of frames is combined as weighted median. We got the master bias frame from the set of bias frames and subtract it from all other frames. We made a master flat-field frame by the same task (imcombine) from the set of flat frames.

### 3.3 Aperture extraction and flat fielding

We can see in Fig. 3.1 that the light from the spectrograph on the CCD frame is divided into individual stripes called apertures. Apertures have ladderlike structure, thus the frame can be called echellogram. Every aperture has a bit different, curved shape in the echellogram. We have to trace the shape of every aperture to add the flux from the individual pixels perpendicular to the course of the aperture. The typical shape of one of the apertures is shown in Fig. 3.3. We define and extract apertures from two-dimensional CCD frame by task "apall". This procedure allows us to trace profiles of all apertures similarly to the one shown in Fig. 3.3. Settings of the apall task are available in the appendix in Fig. 4.11. We used Chebyshev polynomials as it is a default fitting technique of this task, other functions such as Legendre polynomials or spline degree 3 interpolations are also available. We can see all identified apertures that were successfully fitted in Fig. 3.4. By extracting the apertures from the scientific object frame in Figure 3.1, we created a template, which we then use to extract and create a normalized flat. Because the echellogram is stable for a long time, we create such a template for every night and then use it to extract all the apertures from all the frames from that night including the master flat and ThAr frames.

Due to the properties of the spectrograph, the apertures are not evenly illuminated. We

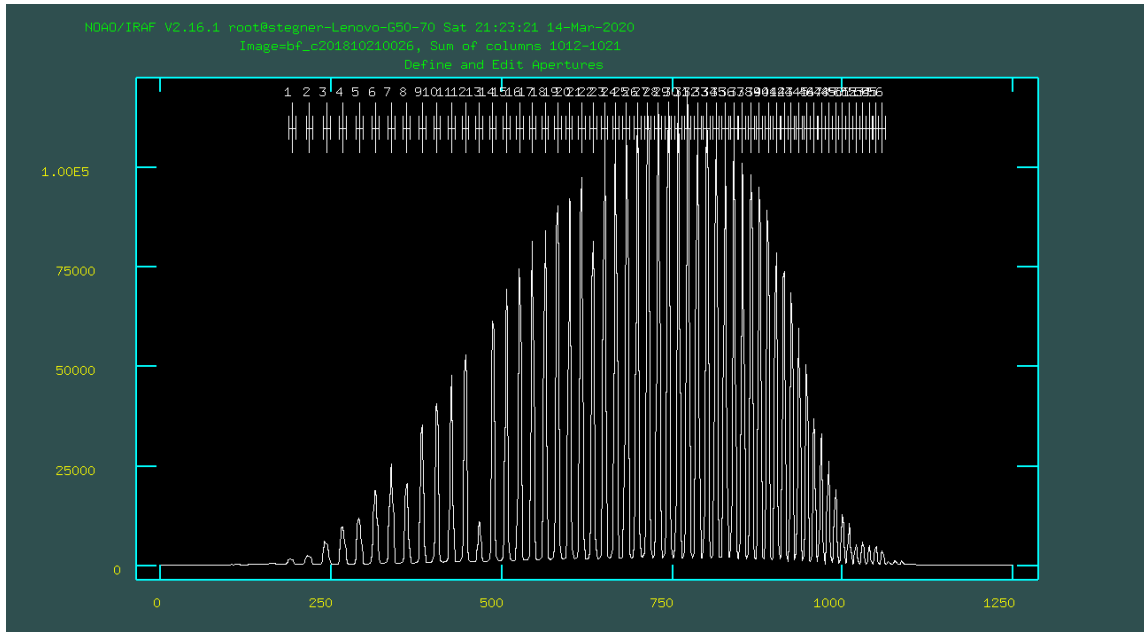


Figure 3.4: All the traced apertures of a  $\alpha$  Lyr frame. The horizontal axis represents the columns and vertical axis represents relative flux. Frame taken on October, 21 2018 from the IRAF environment.

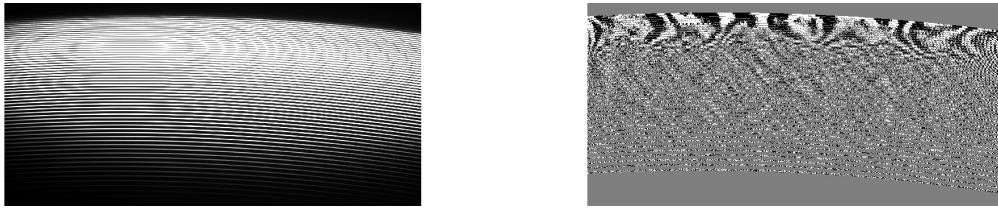


Figure 3.5: Comparing the master flat frame with and without normalization. Frame taken November, 11 2018.

used the task "apflatten" and make the normalized flat frame, that compensates the uneven illumination. We used spline degree 3 interpolation, specific settings are in Fig. 4.12. You can compare the master flat frame with and without normalization in Fig. 3.5. We then divided all frames (scientific and ThAr) by the normalized flat frames by using task called "imarith".

We now extract light from the apertures of the scientific object frames. After the extraction of the light from apertures we got two dimensional spectra having pixels on the horizontal axis and particular spectral orders on the vertical axis (Fig. 3.6). Every pixel contains the sum of extracted flux from pixels in aperture.

### 3.4 Wavelength calibration

Because the extracted spectra have pixels on the horizontal axis, we need to calibrate pixels to wavelengths. This is why we made ThAr comparison spectra, with emission

peaks on the known wavelengths. An example showing a green part of the visible light spectrum is shown in Fig. 3.7. We need to identify these emission peaks in the extracted orders and determine relation between pixels and wavelength by using task "ecidentify". For the identification of the emission lines we used the catalogue prepared for the OES by Marek Skarka. You can see an example of the identification of the peaks in Fig. 3.8 and settings of the task in Fig. 4.13 in the appendix. Once we determined the pixel-wavelength relation, we converted pixels to wavelengths of all the object spectra by using task "dispcor".

### 3.5 Normalization of the spectra

The next step is to normalize scientific spectra. We use the task "continuum". This part of extraction proces is strongly influenced by human factor. Task settings are shown in Fig. 4.14 in the appendix. Important settings are naverage, function and order. Naverage represents the average number of sample points to be combined to create a fitting point. The fitted function can be a Legendre polynomial, Chebyshev polynomial, linear spline, or cubic spline of a given order or number of spline pieces. The order represents the order of the polynomials or the number of spline pieces. The process is shown in Fig. 3.9. Normalization is made for each order separately.

### 3.6 One dimensional spectrum production and its final corrections

Task "sarith" than divides frames without fitted continuum by those with fitted continuum and get a pure continuum of every aperture. As a next step, we combine frames without fitted continuum into one-dimensional frames and the same with the pure continuum frames. We then divide one-dimensional frames without fitted continuum by one-dimensional frames with pure continuum information, that finally gives us one-dimensional scientific

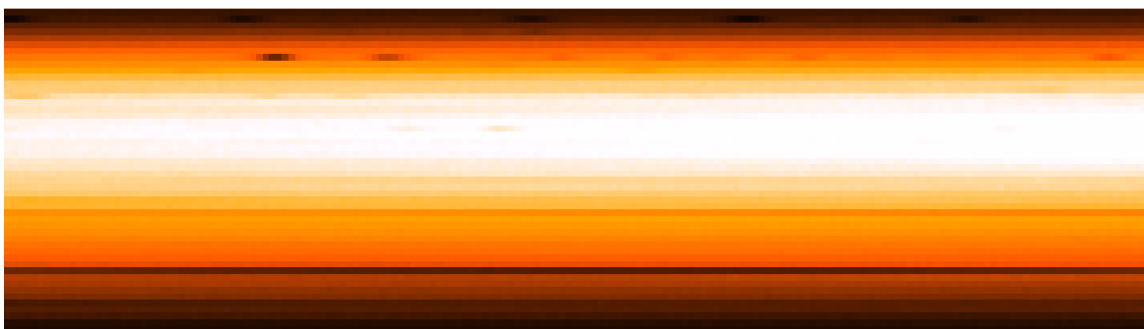


Figure 3.6: Detail of an  $\alpha$  Aquale (Altair) frame showing part of the extracted orders. Some lines are visible in the left top segment.

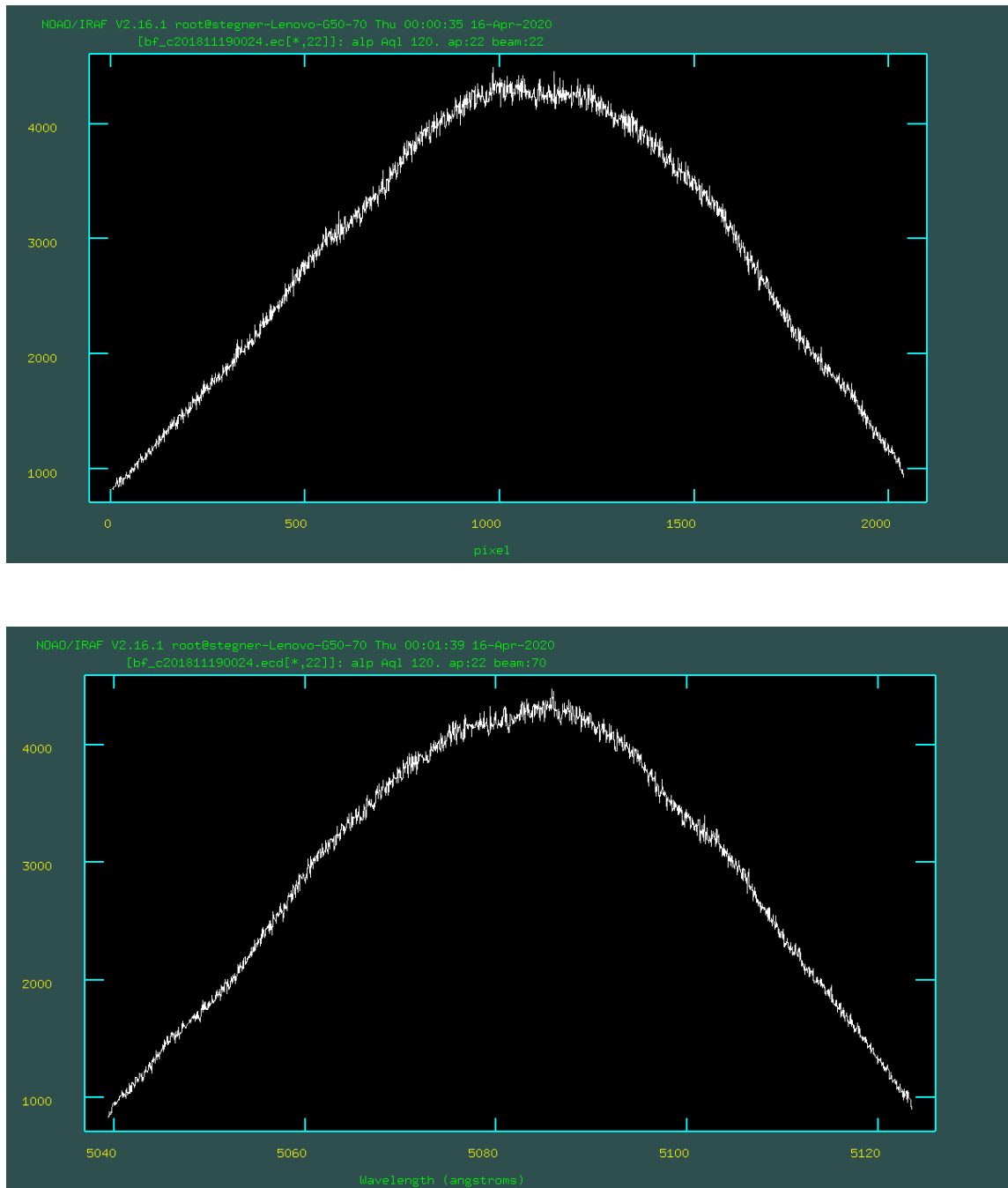


Figure 3.7: The green part of the visible light spectrum of  $\alpha$  Aquale, before and after the wavelength calibration (Sec. 3.4) in the IRAF environment.

spectrum like the one shown in Fig. 3.10. This spectrum needs to be corrected from systematics made during the merging of the spectrum. We then have to remove drops in red part of spectra caused by the fact that orders do not overlap there. The best way to remove the drops is by replacing the zero values with the value with 1 using an automatic script.

To get the final spectrum for further work, it is necessary to perform the so called Heliocentric correction that shifts the whole spectrum in the way that the movement of the Earth around the Sun and the rotation of the Earth is eliminated. Or, better said, it eliminates the Doppler shift caused by these effects. Heliocentric correction is made by task "rvcorrect". Position of the observatory is defined in variable "observatory", where we predefined the parameters of the Ondrejov observatory. Used settings of task "rvcorrect" are in the appendix in Fig. 4.15.

In addition, we correct for the star's own motion in space, by its intrinsic radial velocity determined from the shifts of the spectral lines equation 1.8. Radial velocity correction is made by the task "dopcor". The obtained velocities in Table 3.1 are measured only from the positions of Balmer spectral lines. The low number of used lines causes that our radial velocity values are only very rough estimates. That is why we used the radial velocity values listed in column 3 in Table 3.1 from the literature. Used settings of task "rvcorrect" are in the appendix in Fig. 4.16. The final spectra in the fits format are available online as a supporting material.

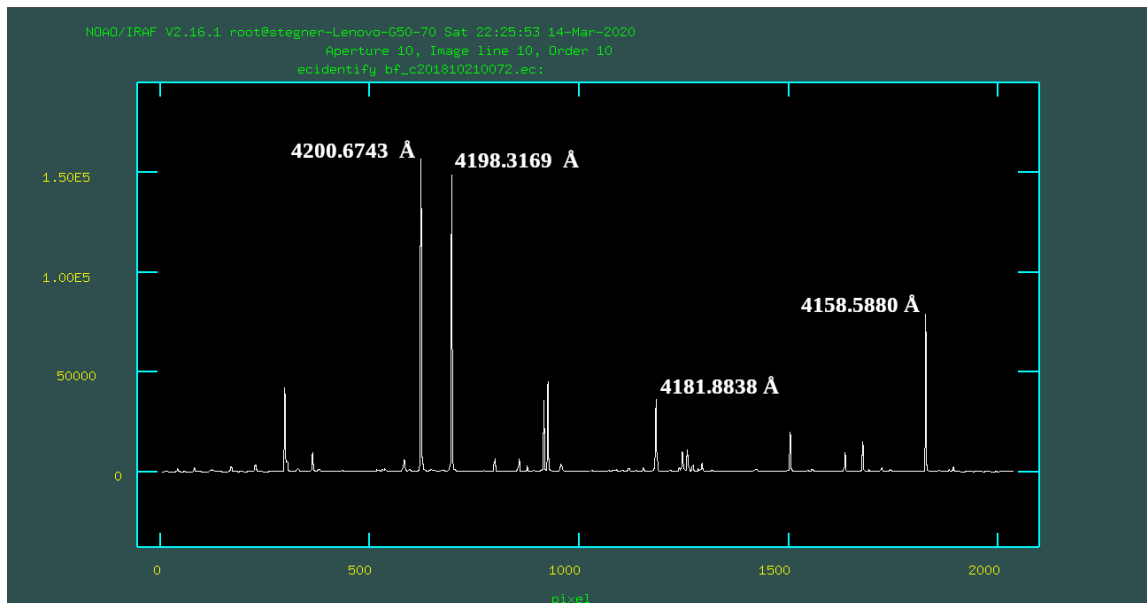


Figure 3.8: Identification of the ThAr emission lines in aperture 10.

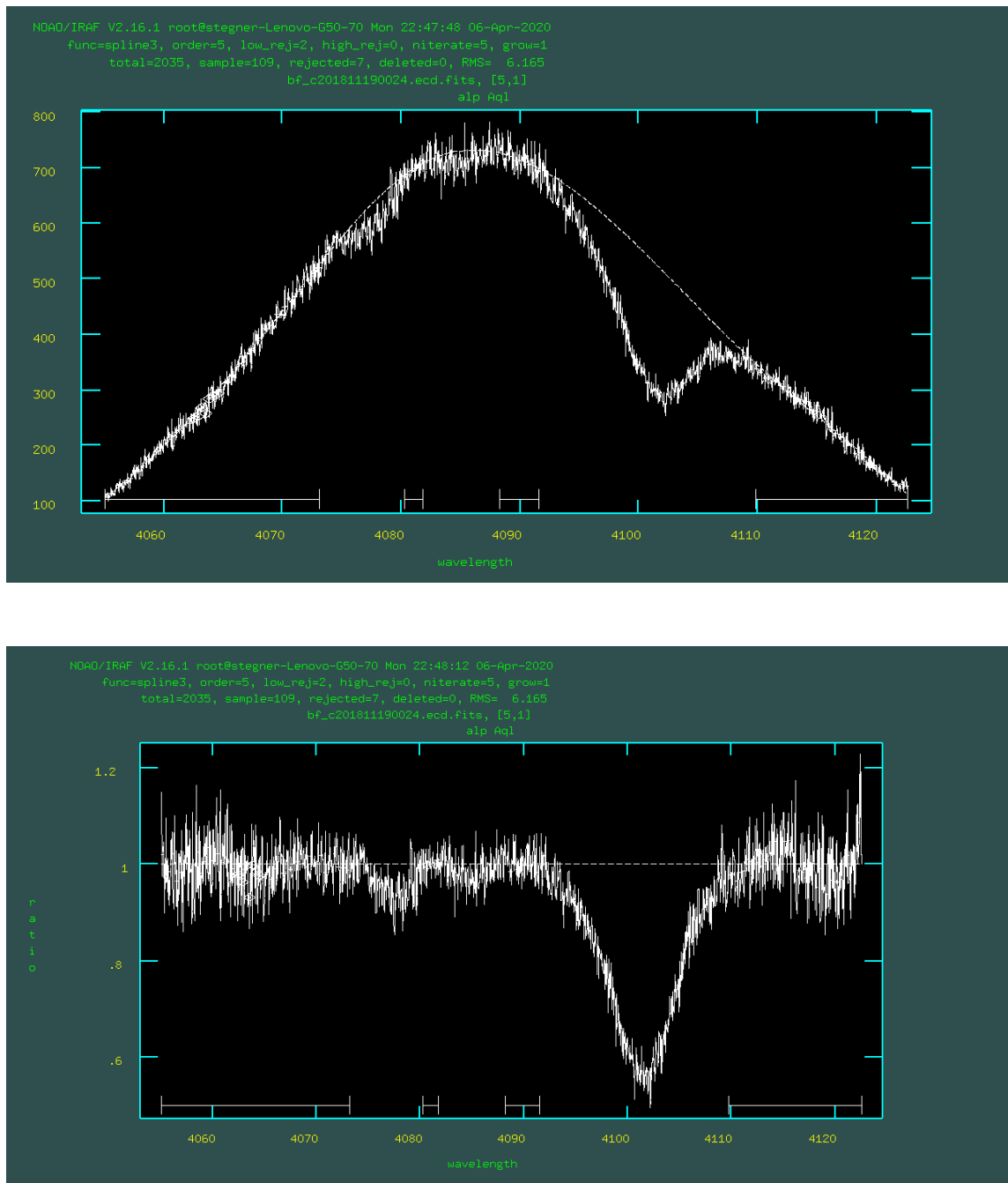


Figure 3.9: Spectrum before (top panel) and after normalization (bottom panel). The horizontal axis represents the wavelength in Angströms, the vertical axis is different for each frame, the dashed line is the fit of the continuum, and the horizontal lines are the areas used for the fit of the continuum.

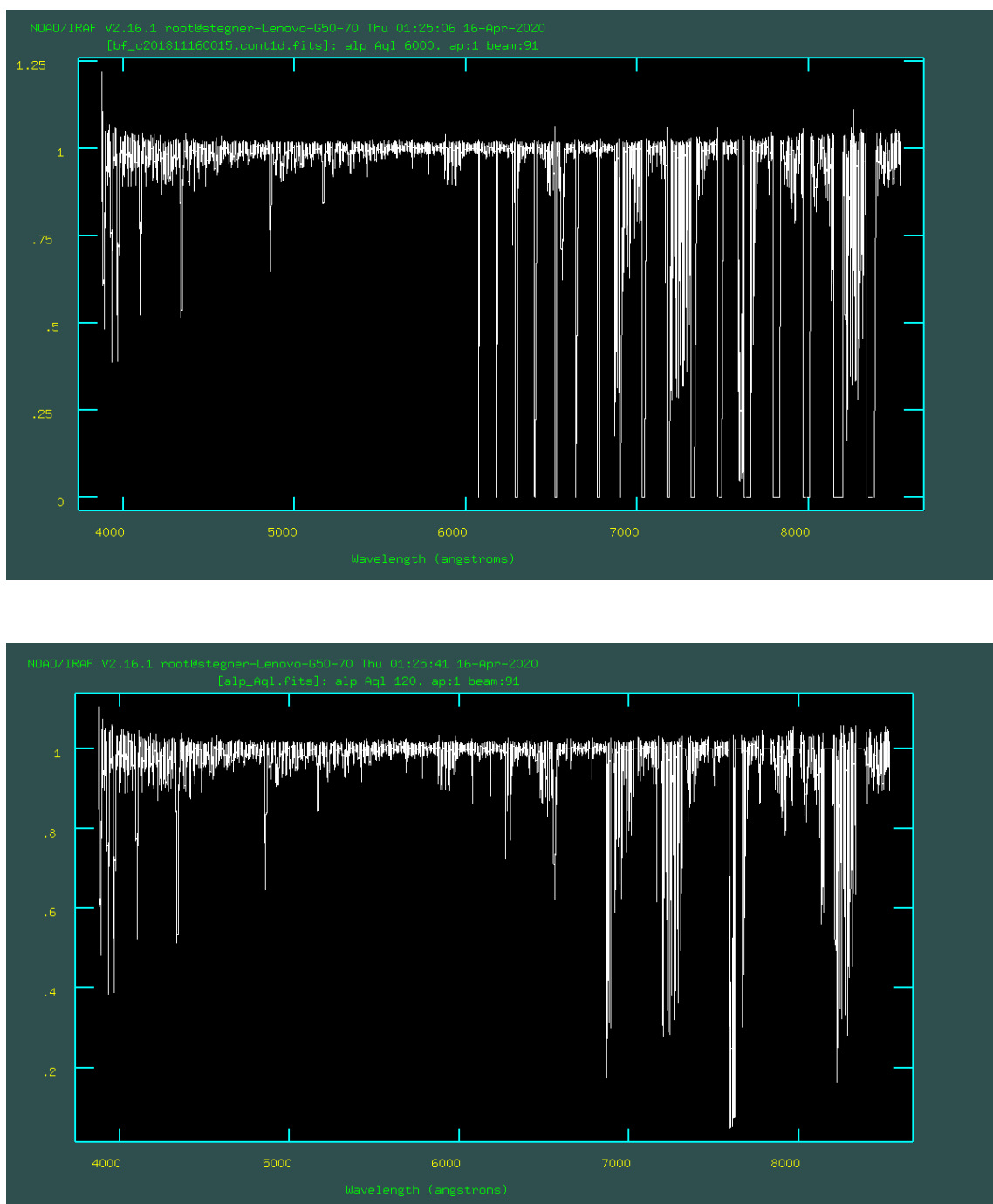


Figure 3.10: Final 1-d spectrum before the artificial flux drops are removed (top panel) and after their removal (bottom panel). Strong features behind 6900 Å are telluric lines.

Table 3.1: Radial velocities obtained from Balmer spectral lines  $H\alpha$  (6563),  $H\beta$  (4861),  $H\gamma$  (4340) and  $H\delta$  (4102) are in column 1. Radial velocities from [e9 \(2020\)](#) are in column 2. For the calculation of the errors we adopted student coefficient corresponding to the reliability level of 0.6827.

STAR	Measured $v_{\text{radial}}$ [ $\frac{\text{km}}{\text{s}}$ ]	Simbad $v_{\text{radial}}$ [ $\frac{\text{km}}{\text{s}}$ ]
10 Lac	$-12.1 \pm 0.8$	$-10.1 \pm 0.3$
$\eta$ Aur	$1 \pm 3$	$7.3 \pm 0.7$
HD 14372	$1.0 \pm 0.7$	$0.1 \pm 0.8$
$\alpha$ Lyr	$-20 \pm 3$	$-20.6 \pm 0.2$
$\delta$ Leo	$-18 \pm 2$	$-20.9 \pm 0.6$
$\alpha$ Aql	$-25 \pm 4$	$-26.6 \pm 0.4$
49 UMa	$3.3 \pm 0.7$	$3 \pm 2$
HD 6301	$1.0 \pm 0.6$	$1.5 \pm 0.3$
HD 10874	$-6 \pm 3$	$-3 \pm 2$
HD 109358	$4 \pm 4$	$6.268 \pm 0.001$
HD 168009	$-67 \pm 2$	$-64.597 \pm 0.003$
HD 193664	$-4 \pm 1$	$-4.455 \pm 0.001$
HD 71148	$-34 \pm 1$	$-32.368 \pm 0.003$
54 Psc	$-27 \pm 2$	$-32.898 \pm 0.001$
HD 84035	$-13 \pm 1$	$-12.158 \pm 0.002$
BD+63 869	$16 \pm 2$	$15.485 \pm 0.001$

# Chapter 4

## OES spectral atlas

It can be seen at first glance in Fig. 4.1 that the spectra of different spectral type stars differ. Particular spectral types are discussed in separate sections.

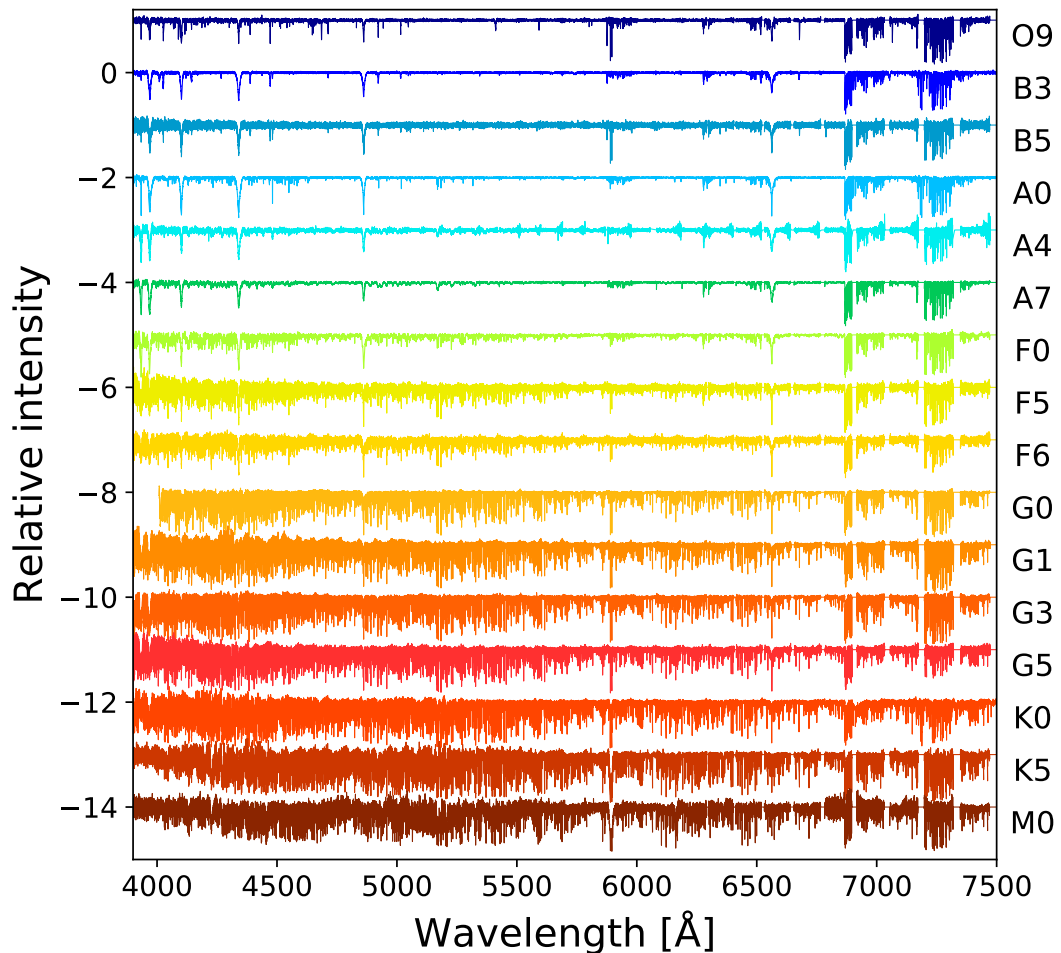


Figure 4.1: All the acquired spectra. From spectral type O9 star 10 Lac in the top to the spectral type M0 star BD+63 869 in the bottom. Spectral types are shown in the right-hand edge of the figure.

## 4.1 Spectral type O – 10 Lac

For the O-type stars, the most indicative feature is the ratio between He II (4541) and He I (4471) (see the top left panel of Fig. 4.2) lines, that varies with decreasing temperature. He I (4471) line decrease its strength with decreasing temperature till a complete disappearance in B3 stars (see the top left panel of Fig. 4.2). The star 10 Lac (O9 type) has a distinct He II (4541) line, while  $\eta$  Aur (B3 type) shows no He II (4541) line.

Another feature that can be used for the classification of O-type stars is the ratio between He I (4387) and He I (4144) lines (see the top right-hand panel of Fig. 4.2). He I (4387) dominate till the O9 type, where the He I lines equal, which is not the case for our spectrum of the 10 Lac (O9 type), where the He I (4387) line is still dominant.

The ratio between Si II (4128-4130) (see the bottom panel of Fig. 4.2) and Si III (4552) can indicate that we are approaching cooler stars than O9, because detectability of the Si II (4128-4130) increases with decreasing effective temperature (Gray & Corbally, 2009). The Si II (4128-4130) lines are hardly visible in the spectrum of the 10 Lac (O9 type), but are apparent in the spectrum of the  $\eta$  Aur in the bottom panel of Fig. 4.2.

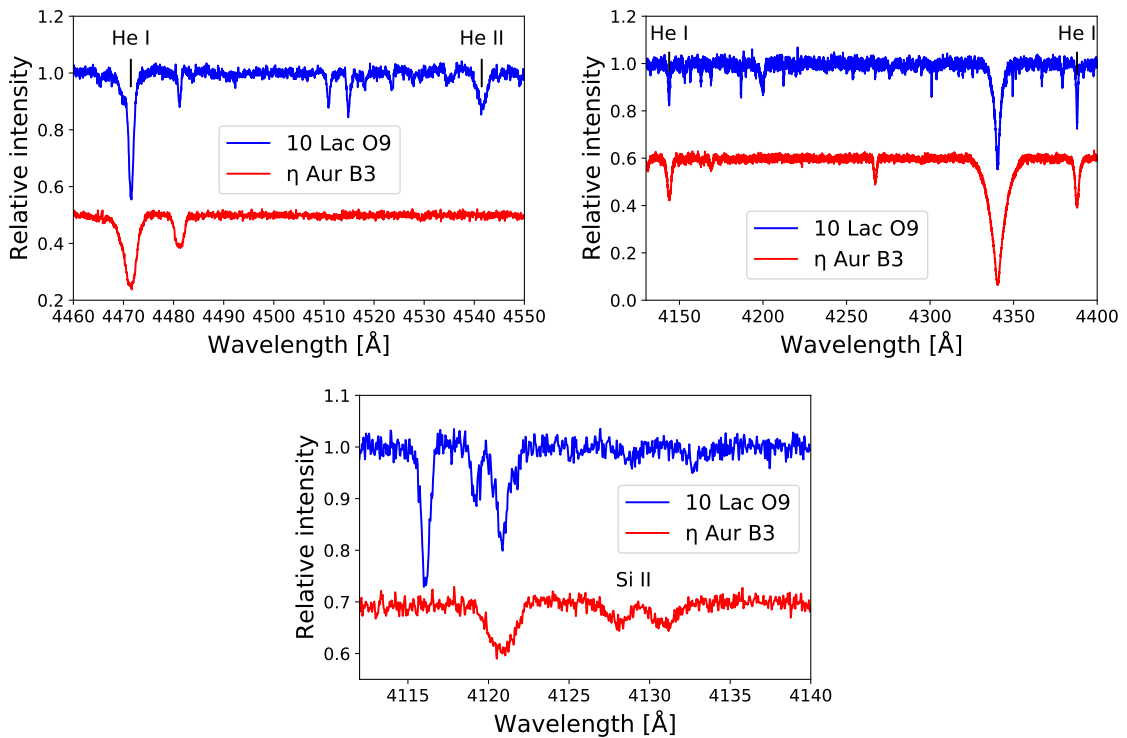


Figure 4.2: Regions defining the O type stars. The figures compare 10 Lac (O9) and  $\eta$  Aur (B3) stars. He II (4541) and He I (4471) region. He I (4387) and He I (4144) region. Si II (4128-4130) region. The spectrum of  $\eta$  Aur was shifted for better visibility.

## 4.2 Spectral type B – $\eta$ Aur, HD 14372

He I lines are in general strongest in B2 types (e4, 2020). The ratio between Si III (4552) and Si II (4128-4130) lines can be used for identification of the B type star because the Si III (4552) slowly weakens with decreasing temperature and the Si II (4128-4130) line is getting stronger (see the left panel of Fig. 4.3). The presence of the Mg II (4481) line, that appears in spectral type B0 and strengthens with lower temperatures, also indicates a B type star. The ratio between He I (4471) and Mg II (4481) in the right-hand panel of Fig. 4.3 is the best indicator from early B type stars because the He I (4471) line fades until disappearing at the A0 level (Gray & Corbally, 2009). We see that the Mg II (4481) and Si II (4128-4130) lines are strengthening from the B3 type ( $\eta$  Aur) through B5 type (HD 14372) to A0 ( $\alpha$  Lyr) in Fig. 4.3.

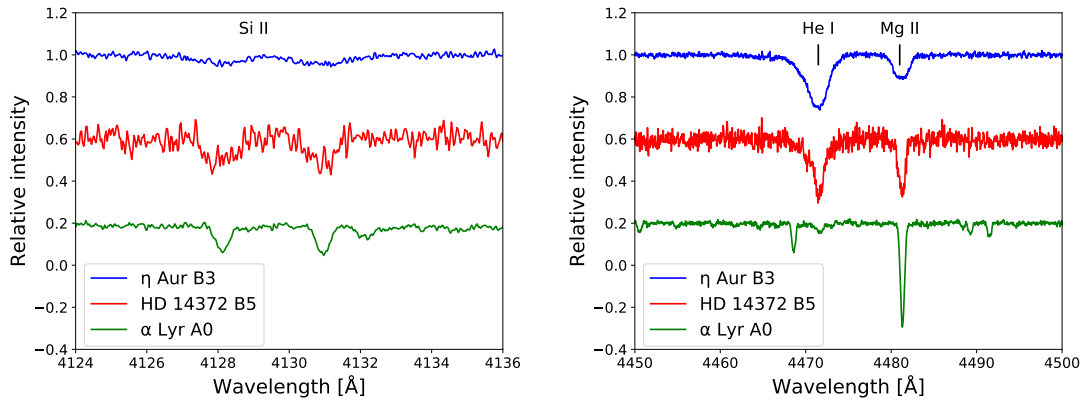


Figure 4.3: Regions defining the B type stars. He I (4471) and Mg II (4481) region. Si II (4128-4130) region. HD 14372 and  $\alpha$  Lyr spectra were shifted for better visibility.

## 4.3 Spectral type A – $\alpha$ Lyr, $\delta$ Leo, $\alpha$ Aql

Balmer hydrogen lines are in general strongest in A0 types, that is represented by  $\alpha$  Lyr, and slowly fade towards lower temperatures. (e4, 2020) There are strong Balmer lines and almost no He I lines. Balmer lines are on their broad maximum at A2 type. We compare Balmer lines in  $\alpha$  Lyr (A0 type) with the lines of  $\delta$  Leo (A4 type) and  $\alpha$  Aql (A7 type), where the lines are weaker (see the left panel of Fig. 4.4). Later types of A stars can be identified by the ratio between H $\delta$  (4102) and H $\epsilon$  (3970) lines in the top panel of Fig. 4.4, that is slowly decreasing with lower temperatures, because the H $\delta$  (4102) line weakens. Strength of H $\alpha$  also decreases with decreasing temperature. Ca II K (3934) line in the right-hand panel of Fig. 4.4 dramatically increases towards cooler types, but it is on the edge of detectability of OES, because of its low signal, so we have to be careful and not put big importance in it (Gray & Corbally, 2009).

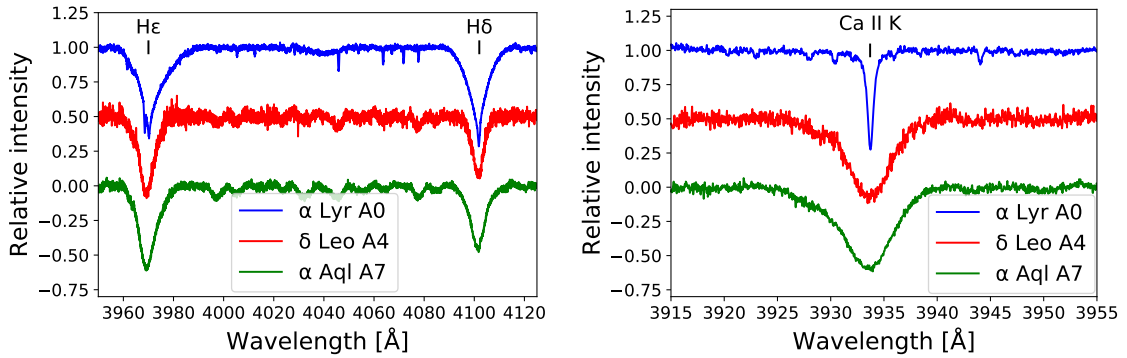


Figure 4.4: Regions defining the A type stars. H $\delta$  (4102) and H $\epsilon$  (3970) region. Ca II K (3934) region.  $\delta$  Leo and  $\alpha$  Aql spectra were shifted for better visibility.

#### 4.4 Spectral type F – 49 UMa, HD 6301, HD 10874

Although the strength of the Ca II K (3934) line is mostly constant (see the top left panel of Fig. 4.5) in the F type stars, difference in shape of the line between the 49 UMa (F0 type) spectrum and the HD 6301 (F5 type) and HD 10874 (F6 type) spectra is really dramatic.

Ca I (4226) line grows rapidly with decreasing temperature and F5 type stars such as HD 6301 can be identified by the dominance of this line between H $\gamma$  (4340) and H $\delta$  (4102) lines (see the top right-hand panel of Fig. 4.5).

Metallic lines strengthen with decreasing temperature and become a great spectral type indicators for F5 and cooler type stars. Thus the ratios such as Fe I (4046)/H $\delta$  (4102) (see the bottom left panel of Fig. 4.5), Ca I (4226)/H $\delta$  (4102) H $\gamma$  (4340) (see the top left panel of Fig. 4.5) and Fe I (4383)/H $\gamma$  (4340) (see the bottom right-hand panel of Fig. 4.5) are best for the spectral classification in this spectral type range (Gray & Corbally, 2009). Star HD 10874 (F6) has the most visible metallic lines of our F type stars sample (see the bottom right-hand panel of Fig. 4.5).

#### 4.5 Spectral type G – HD 109358, HD 168009, HD 193664, HD 71148

G-type stars show steady fade of the Balmer lines. Metallic lines start to increase, mainly the resonance Ca I (4226) in the top left panel of Fig. 4.6 grows gradually until the early (hottest) K-types. We can not see the Ca I (4226) line in HD 109358 (G0 type) spectrum, the first trace of the line comes with G1-type star HD 168009. The iron lines increase their strength with lower temperature in G-type stars. Thus the ratios of Fe I (4046)/H $\delta$  (4102), Fe I (4144)/H $\delta$  (4102) and Fe I (4383)/H $\gamma$  (4340) (see the top right-hand panel of Fig. 4.6) are best for the spectral classification in this range. Increasing strength of Mg I (5167, 5172, 5183) triplet (see the bottom panel of Fig. 4.6), that is weakest in the HD 109358 (G0 type) spectrum and strongest in the HD 71148 (G5 type<sup>1</sup>) spectrum is a good criteria for classification of the G-type stars too (Gray & Corbally, 2009).

<sup>1</sup>(e9, 2020) states a different (G1V) spectral type than the original source.

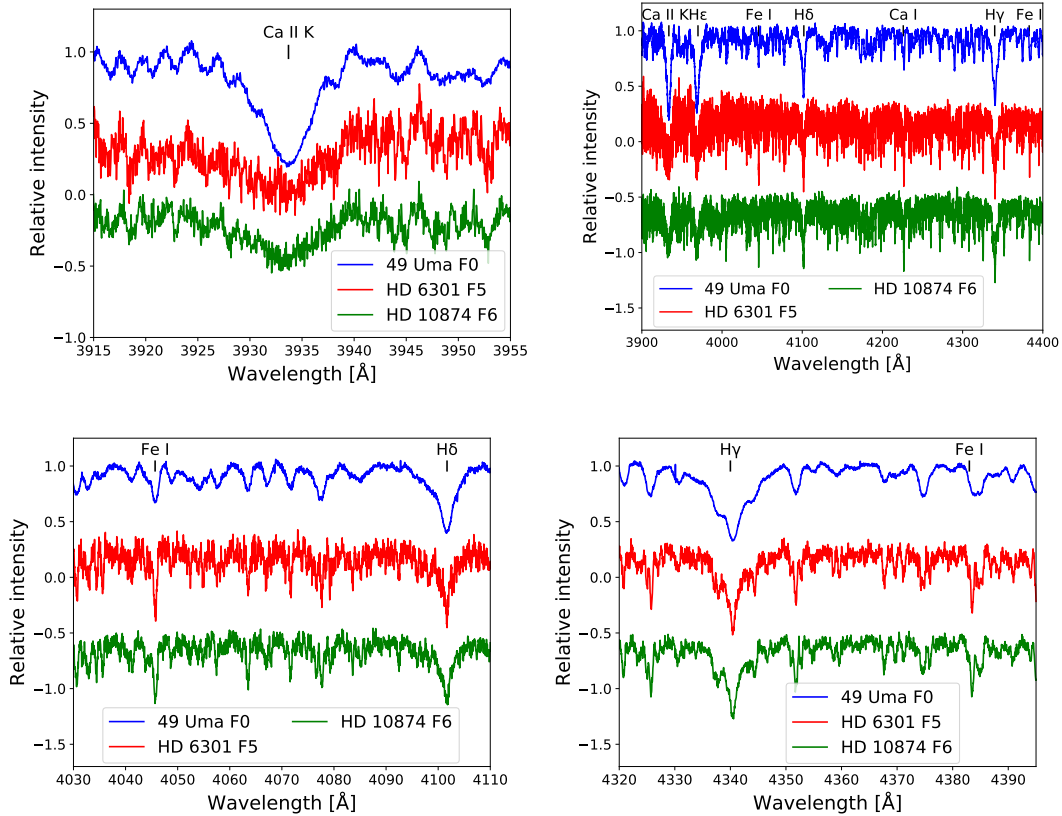


Figure 4.5: Regions defining the F type stars. Ca II K (3934) region. H $\epsilon$  (3970), Fe I (4046), Ca I (4226), H $\gamma$  (4340), H $\delta$  (4102), Fe I (4383) region. Fe I (4046) and H $\delta$  (4102) region. Fe I (4383), H $\gamma$  (4340) region. HD 6301 and HD 10874 spectra were shifted for better visibility.

## 4.6 Spectral type K – 54 Psc, HD 84035

For a rough identification of a K-type star, the ratios between Fe I, Ca I/Hydrogen lines are considered to be the best indicator because hydrogen lines are getting fainter with decreasing the temperature. Ca I (4226) line becomes dramatically stronger by mid-K types. Ratios between Cr I (4254, 4275, 4290) triplet in the left panel of Fig. 4.7 plays important role in the identification of K-type stars because Cr I lines should get more dominant with decreasing the temperature, which is obvious from the difference between the 54 Psc (K0 type) spectrum and the HD 84035 (K5 type) spectrum. The ratio between H $\alpha$  (6563) and a blend (Fe I, Ti I, Cr I, Ba I, Ca I, Mn I, Co I and Ni I (Turnshek et al., 1985)) at 6497 Å (see the right-hand panel of Fig. 4.7), can also be very useful for K-type star identification (Gray & Corbally, 2009).

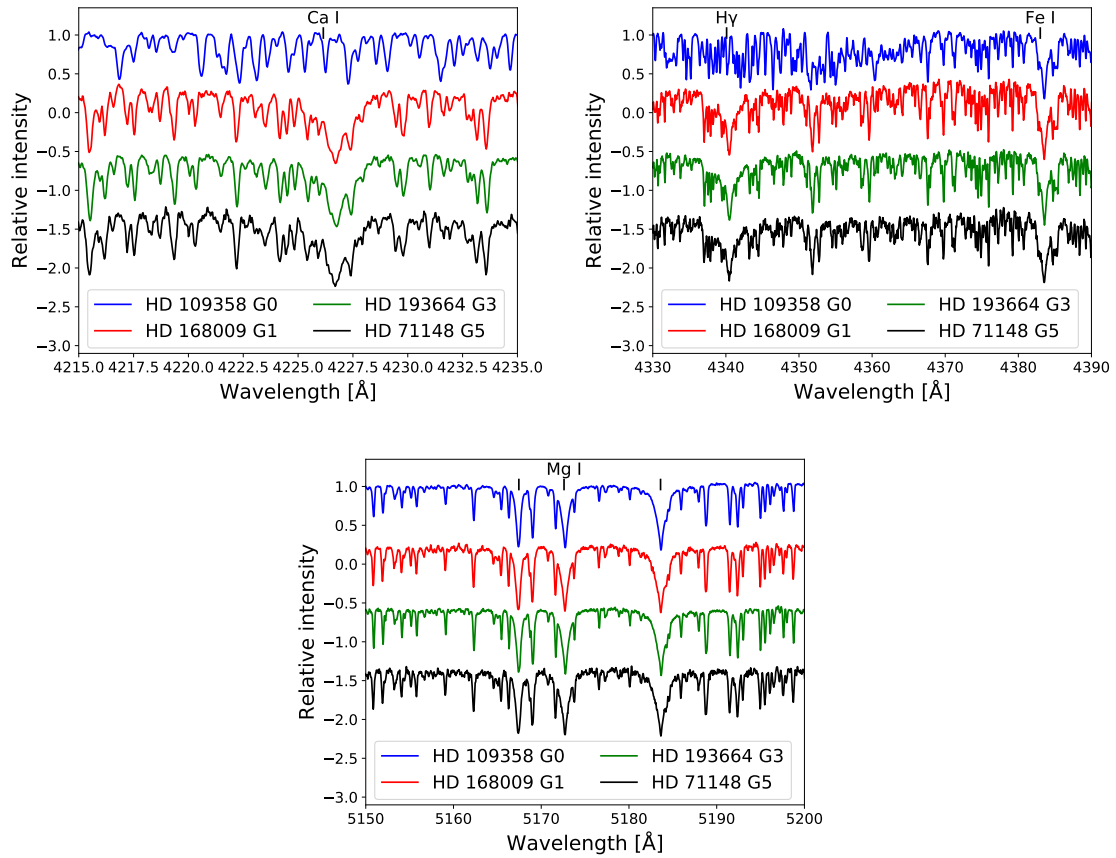


Figure 4.6: Regions defining the G-type stars. Mg I (5167, 5172, 5183) triplet region. Ca I (4226) region. Fe I (4383), H $\gamma$  (4340) region. HD 168009, HD 193664 and HD 71148 spectra were shifted for better visibility.

## 4.7 Spectral type M – BD+63 869

Na I doublet (5890, 5896) broadening in the top left panel of Fig. 4.8 can be a good indicator of M-type stars (e4, 2020). We see a huge difference between Na I doublet in BD+63 869 (M0 type) spectrum and in the HD 84035 (K5 type) spectrum. We should also check the Ca I (4226)/Fe I (4383) ratio if we are in the suspicion of the M-type star because the iron line is rapidly losing its strength with decreasing temperature. We see the difference between the two metallic lines in BD+63 869 (M0 type) spectrum and HD 84035 (K5 type) spectrum in the top right-hand panel of Fig. 4.8 is good indication of M-type star. Strengthening of TiO (4804, 4955, 5166) lines (see the bottom panel Fig. 4.8) can also indicate M-type star. The Cr I (4254, 4275, 4290) triplet in the bottom panel of Fig. 4.8 loses its intensity with decreasing temperature in M-type stars. (Gray & Corbally, 2009)

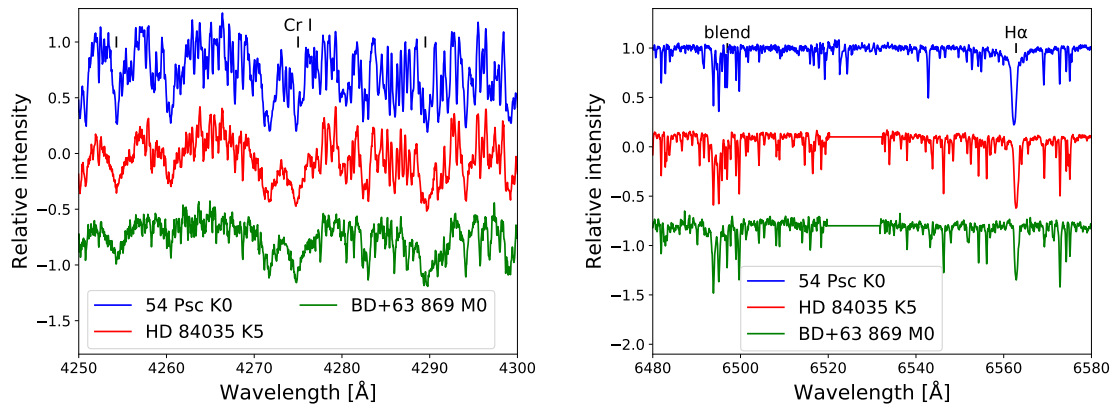


Figure 4.7: Regions defining the K-type stars. Cr I (4254, 4275, 4290) triplet region.  $H\alpha$  (6563) and a metallic blend at 6497 region. HD 84035 and BD+63 869 spectra were shifted for better visibility.

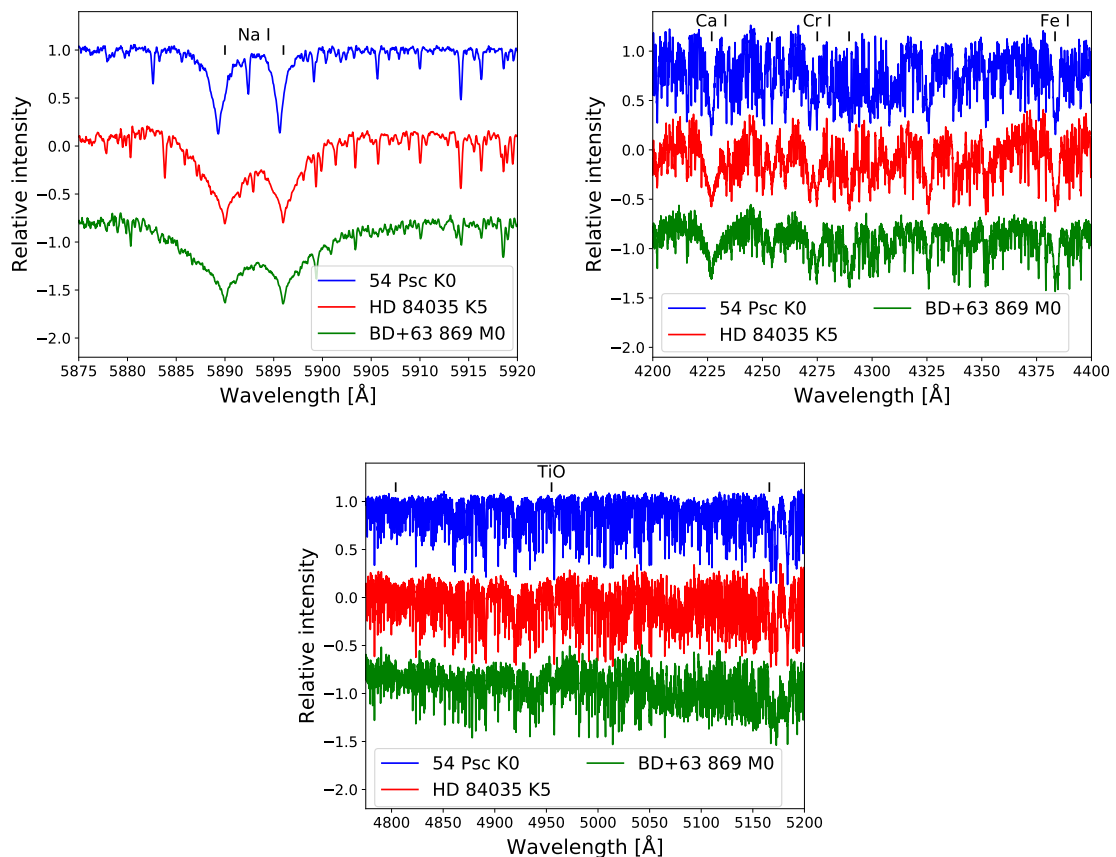


Figure 4.8: Regions defining the M-type stars. Na I doublet (5890, 5896) region. TiO (4804, 4955, 5166) region. Ca I (4226), Fe I (4383) and Cr I (4254, 4275, 4290) triplet region. HD 84035 and BD+63 869 spectra were shifted for better visibility.

# Conclusions

The main goal of this thesis was to make spectral atlas for Ondřejov Echelle Spectrograph (OES) mounted on the 2m Perek telescope located in the Czech Republic. For that purpose, we selected sixteen main sequence stars according to the criteria corresponding to the limits of the used instrument and telescope. We observed one O-type star, two B-type stars, three A-type stars, three F-type stars, four G-type stars, two K-type stars, and one M star.

Stars were measured over ten nights during 2018 and 2019 in collaboration with nine observers. The brightness ranged from 0.03 to 9.18 mag and the exposure times from 60 s to 3600 s. The signal to noise ratio of the obtained spectra was between 33 and 230. In addition to the star frames, different sets of calibration frames were also taken.

The obtained frames were fully reduced by software package IRAF. The frames were corrected of bad pixels, bad regions, cosmic rays and other defects. All the scientific and comparison ThAr frames were bias subtracted and flatfielded. From the CCD frame, the apertures were traced and the flux was extracted. Subsequently, the science spectra were calibrated to the wavelengths and normalized to the unity and combined to 1-d spectrum. Finally, we removed bad parts of the spectra caused by non-overlapping spectral orders and shifted all the spectra to the laboratory rest frame by using radial velocities from the Simbad database.

For each of the studied stars, we investigated the characteristic regions of the spectra for particular spectral classes and compared them. Our study confirms classification of the stars in the literature. Our efforts led to the creation of a spectral atlas that can be used for a fast classification of stars observed by OES.

# References

- Appenzeller, I. 2013, Introduction to Astronomical Spectroscopy
- Aufdenberg, J. P., Mérand, A., Coudé du Foresto, V., et al. 2006, *The Astrophysical Journal*, 645, 664
- Catanzaro, G. 2014, Determination of Atmospheric Parameters of B, 97
- Cowley, A. P. 1976, *Publications of the Astronomical Society of the Pacific*, 88, 95
- Gray, R. O. 1985, *Journal of the Royal Astronomical Society of Canada*, 79, 237
- Gray, R. O. 1988, *Journal of the Royal Astronomical Society of Canada*, 82, 336
- Gray, R. O., & Corbally, C. 2009, *Stellar Spectral Classification by Richard O. Gray and Christopher J. Corbally*. Princeton University Press
- Gray, R. O., & Garrison, R. F. 1987, *The Astrophysical Journal Supplement Series*, 65, 581
- Grossová, R. 2016, arXiv e-prints, arXiv:1602.04401 [Diploma thesis]
- Gulliver, A. F., Adelman, S. J., Cowley, C. R., et al. 1991, *The Astrophysical Journal*, 380, 223
- Hoffleit, D., & Jaschek, C. 1991, New Haven
- Kirchhoff, G., & Bunsen, R. 1860, *Annalen der Physik*, 186, 161
- Koubský, P., Mayer, P., Čáp, J., et al. 2004, *Publications of the Astronomical Institute of the Czechoslovak Academy of Sciences*, 92, 37
- Mikulášek Z., Krtička J. 2005, *Základy fyziky hvězd*, ÚTFA PřF MU, Brno [Textbook]
- Newton, I. 1671, *Philosophical Transactions of the Royal Society of London Series I*, 6, 3075
- Peterson, D. M., Hummel, C. A., Pauls, T. A., et al. 2006, *Nature*, 440, 896
- Petrie, R. M. 1964, *Publications of the Dominion Astrophysical Observatory Victoria*, 12, 317
- Turnshek, D. E., Turnshek, D. A., & Craine, E. R. 1985, *Astronomy and Astrophysics Series*

**Electronic sources**

- [e1] <https://www.sciencehistory.org/historical-profile/robert-bunsen-and-gustav-kirchhoff>
- [e2] <http://www.ph.surrey.ac.uk/astrophysics/files/spectroscopy.html>
- [e3] <https://stelweb.asu.cas.cz/~slechta/OES/pro-ian/>
- [e4] [https://www.astro.princeton.edu/~burrows/classes/204/stellar\\_atmospheres.HR.pdf](https://www.astro.princeton.edu/~burrows/classes/204/stellar_atmospheres.HR.pdf)
- [e5] [https://en.wikipedia.org/wiki/Stellar\\_classification](https://en.wikipedia.org/wiki/Stellar_classification)
- [e6] <https://stelweb.asu.cas.cz/~slechta/2m/>
- [e7] <http://www.solstation.com/stars3/100-ks.htm>
- [e8] <http://ast.noao.edu/data/software>
- [e9] <http://simbad.u-strasbg.fr/simbad/>

# Appendix

```

                                     I R A F
Image Reduction and Analysis Facility
PACKAGE = proto
  TASK = fixpix

images = []      @all.list  List of images to be fixed
masks =          badpixmask  List of bad pixel masks
(linterp=       INDEF)  Mask values for line interpolation
(cinterp=       INDEF)  Mask values for column interpolation
(verbose=       yes)  Verbose output?
(pixels =       yes)  List pixels?
(mode =        ql)
```

Figure 4.9: Parameters of the "fixpix" task.

```

IRAF
Image Reduction and Analysis Facility
PACKAGE = immatch
TASK = imcombine

input = @b_flat.list List of images to combine
output = mflat List of output images
(headers= ) List of header files (optional)
(bpmasks= ) List of bad pixel masks (optional)
(rejmask= ) List of rejection masks (optional)
(nrejmas= ) List of number rejected masks (optional)
(expmask= ) List of exposure masks (optional)
(sigmas = ) List of sigma images (optional)
(imcmb = $I) Keyword for IMCMB keywords
(logfile= STDOUT) Log file

(combine= median) Type of combine operation
(reject = sigclip) Type of rejection
(project= no) Project highest dimension of input images?
(outtype= real) Output image pixel datatype
(outlimi= ) Output limits (x1 x2 y1 y2 ...)
(offsets= none) Input image offsets
(masktyp= none) Mask type
(maskval= 0) Mask value
(blank = 0.) Value if there are no pixels

(scale = none) Image scaling
(zero = none) Image zero point offset
(weight = none) Image weights
(statsec= ) Image section for computing statistics
(expname= ) Image header exposure time keyword

(lthresh= INDEF) Lower threshold
(hthresh= INDEF) Upper threshold
(nlow = 1) minmax: Number of low pixels to reject
(nhigh = 1) minmax: Number of high pixels to reject
(nkeep = 1) Minimum to keep (pos) or maximum to reject (neg)
(mclip = yes) Use median in sigma clipping algorithms?
(lsigma = 3.) Lower sigma clipping factor
(hsigma = 3.) Upper sigma clipping factor
(rdnoise= 0.) ccdclip: CCD readout noise (electrons)
(gain = 1.) ccdclip: CCD gain (electrons/DN)
(snoise = 0.) ccdclip: Sensitivity noise (fraction)
(sigscal= 0.1) Tolerance for sigma clipping scaling correction
(pclip = -0.5) pclip: Percentile clipping parameter
(grow = 0.) Radius (pixels) for neighbor rejection
(mode = ql)

```

Figure 4.10: Parameters of the "imcombine" task.

```

                                I R A F
                                Image Reduction and Analysis Facility

PACKAGE = echelle
TASK = apall

input = []
(output = Vega List of input images
(apertur= Aper_Template) List of output spectra
(format = 56) Apertures
(referen= echelle) Extracted spectra format
(profile= ) List of aperture reference images
) List of aperture profile images

(interac= yes) Run task interactively?
(find = yes) Find apertures?
(recente= yes) Recenter apertures?
(resize = no) Resize apertures?
(edit = yes) Edit apertures?
(trace = yes) Trace apertures?
(fittrac= yes) Fit the traced points interactively?
(extract= yes) Extract spectra?
(extras = no) Extract sky, sigma, etc.?
(review = no) Review extractions?

(line = INDEF) Dispersion line
(nsum = 10) Number of dispersion lines to sum or median

# DEFAULT APERTURE PARAMETERS

(lower = -5.) Lower aperture limit relative to center
(upper = 5.) Upper aperture limit relative to center
(apidtab= ) Aperture ID table (optional)

# DEFAULT BACKGROUND PARAMETERS

(b_funct= chebyshev) Background function
(b_order= 1) Background function order
(b_sampl= -10:-6,6:10) Background sample regions
(b_naver= -3) Background average or median
(b_niter= 0) Background rejection iterations
(b_low_r= 3.) Background lower rejection sigma
(b_high_= 3.) Background upper rejection sigma
(b_grow = 0.) Background rejection growing radius

# APERTURE CENTERING PARAMETERS

(width = 5.) Profile centering width
(radius = 10.) Profile centering radius

```

Figure 4.11: Parameters of the "apall" task.

```

                                I R A F
                                Image Reduction and Analysis Facility
PACKAGE = echelle
  TASK = apflatten

input  =      mflat List of images to flatten
output =      nflat List of output flatten images
(apertur=    ) Apertures
(referen=    Vega) List of reference images

(interac= 0) yes) Run task interactively?
(find    =  no) Find apertures?
(recente=  yes) Recenter apertures?
(resize  =  no) Resize apertures?
(edit    =  yes) Edit apertures?
(trace   =  no) Trace apertures?
(fittrac=  no) Fit traced points interactively?
(flatten=  yes) Flatten spectra?
(fitspec=  yes) Fit normalization spectra interactively?

(line    =      INDEF) Dispersion line
(nsum    =      10) Number of dispersion lines to sum or median
(thresho=      10.) Threshold for flattening spectra

(pfit    =      fit1d) Profile fitting type (fit1d|fit2d)
(clean   =      no) Detect and replace bad pixels?
(saturat=      INDEF) Saturation level
(readnoi=      10) Read out noise sigma (photons)
(gain    =      2) Photon gain (photons/data number)
(lsigma  =      4.) Lower rejection threshold
(usigma  =      4.) Upper rejection threshold

(funcio= spline3) Fitting function for normalization spectra
(order  =      7) Fitting function order
(sample =      *) Sample regions
(naverag= 1) Average or median
(niterat= 1) Number of rejection iterations
(low_rej= 3.) Lower rejection sigma
(high_re= 3.) High upper rejection sigma
(grow   = 0.) Rejection growing radius
(mode   =      ql)

```

Figure 4.12: Parameters of the "apflatten" task.

```

                                I R A F
                                Image Reduction and Analysis Facility
PACKAGE = echelle
  TASK = eidentify

images = bf_c201810210072.ec Images containing features to be identified
(database= database) Database in which to record feature data
(coordli= linelists$thar_new.dat) User coordinate list
(units = ) Coordinate units
(match = 1.) Coordinate list matching limit in user units
(maxfeat= 2000) Maximum number of features for automatic identific
(zwidth = 10.) Zoom graph width in user units
(ftype = emission) Feature type
(fwidth = 4.) Feature width in pixels
(cradius= 5.) Centering radius in pixels
(thresho= 10.) Feature threshold for centering
(minsep = 2.) Minimum pixel separation
(funcutio= chebyshev) Coordinate function
(xorder = 2) Order of coordinate function along dispersion
(yorder = 2) Order of coordinate function across dispersion
(niterat= 0) Rejection iterations
(lowreje= 3.) Lower rejection sigma
(highrej= 3.) Upper rejection sigma
(autowri= no) Automatically write to database?
(graphic= stdgraph) Graphics output device
(cursor = ) Graphics cursor input
(mode = ql)

```

Figure 4.13: Parameters of the "eidentify" task.

```

                                IRAF
                                Image Reduction and Analysis Facility
PACKAGE = echelle
  TASK = continuum

input  = [] @bf_obj.ecd.list  Input images
output = @bf_obj.cont.list  Output images
(lines = *) Image lines to be fit
(bands = 1) Image bands to be fit
(type = ratio) Type of output
(replace= no) Replace rejected points by fit?
(wavesca= yes) Scale the X axis with wavelength?
(logscal= no) Take the log (base 10) of both axes?
(overrid= no) Override previously fit lines?
(listonl= no) List fit but don't modify any images?
(logfile= logfile) List of log files
(interac= yes) Set fitting parameters interactively?
(sample = *) Sample points to use in fit
(naverag= 10) Number of points in sample averaging
(funcutio= spline3) Fitting function
(order = 7) Order of fitting function
(low_rej= 2.) Low rejection in sigma of fit
(high_re= 0.) High rejection in sigma of fit
(niterat= 5) Number of rejection iterations
(grow = 1.) Rejection growing radius
(markrej= yes) Mark rejected points?
(graphic= stdgraph) Graphics output device
(cursor = ) Graphics cursor input
ask = YES
(mode = ql)

```

Figure 4.14: Parameters of the "continuum" task.

```

IRAF
Image Reduction and Analysis Facility

PACKAGE = rv
TASK = rvcorrect

(files = ) List of files containing observation data
(images = 54_Psc2) List of images containing observation data
(header = yes) Print header?
(input = no) Print input data?
(imupdat= yes) Update image header with corrections?

(epoch = 2000.) Epoch of observation coordinates (years)
(observa= ONDREJOV) Observatory
(vsun = 20.) Solar velocity (km/s)
(ra_vsun= 18.) Right ascension of solar velocity (hours)
(dec_vsu= 30.) Declination of solar velocity (degrees)
(epoch_v= 1900.) Epoch of solar coordinates (years)

(year = ) Year of observation
(month = ) Month of observation (1-12)
(day = ) Day of observation
(ut = ) UT of observation (hours)
(ra = ) Right ascension of observation (hours)
(dec = ) Declination of observation (degrees)
(vobs = 0.) Observed radial velocity
(hjd = ) Heliocentric Julian Day (output)
(vhelio = ) Heliocentric radial velocity (km/s) (output)
(vlsr = ) Local standard or rest radial velocity (km/s) (out
(mode = ql)

```

Figure 4.15: Parameters of the "rvcorrect" task.

```

IRAF
Image Reduction and Analysis Facility

PACKAGE = echelle
TASK = dopcor

input = HD_168009_h.fits List of input spectra
output = HD_168009_cons.fits List of output spectra
redshift= -64.568 Redshift or velocity (Km/s)
(isveloc= yes) Is the redshift parameter a velocity?
(add = yes) Add to previous dispersion correction?
(dispers= yes) Apply dispersion correction?
(flux = no) Apply flux correction?
(factor = 3.) Flux correction factor (power of 1+z)
(apertur= ) List of apertures to correct
(verbose= yes) Print corrections performed?
(mode = ql)

```

Figure 4.16: Parameters of the "dopcor" task.

